

**Exploring the influence of atomic level structure, porosity, and stability of bismuth(III)
coordination polymers on electrocatalytic CO₂ reduction**

Electronic Supplementary Information

*Sara Frank, Erik Svensson Grape, Espen Drath Bøjesen, Rasmus Larsen, Paolo Lamagni, Jacopo
Catalano, A. Ken Inge, Nina Lock*

1. Structure and crystallinity of the pristine coordination polymers

- 1.1.....Synthesis of coordination polymers (CPs)
- 1.2..... Powder X-ray diffraction (PXRD)
- 1.3.....Extended X-ray absorption fine structure (EXAFS) – pristine powders
- 1.4.....Scanning electron microscopy (SEM)
- 1.5.....Transmission electron microscopy (TEM)
- 1.6.....Void space analysis
- 1.7.....Thermogravimetric analysis (TGA) and differential scanning calorimetry (DSC)

2. Electrochemical characterization

- 2.1.....Cyclic voltammetry (CV)
- 2.2.....Reduction peak of bismuth
- 2.3.....Bulk electrolysis
- 2.4.....Overpotentials
- 2.5.....Bulk electrolysis for 1 h and 2 h

3. Structural changes during electrocatalysis

- 3.1.....Scanning electron microscopy (SEM)
- 3.2.....Soaking in the electrolyte KHCO_3
- 3.3.....Transmission electron microscopy (TEM)
- 3.4.....X-ray absorption spectroscopy – linear combination analysis (LCA)
- 3.5.....Grazing incidence X-ray diffraction (GI-XRD)

1. Structure and crystallinity of the pristine coordination polymers

1.1. Synthesis of coordination polymers (CPs)

1.1.1. *Bi(btb)*

A solvothermal synthesis adapted from Lamagni *et al.*¹ and Feyand *et al.*² was used to synthesize *Bi(btb)*, also known as CAU-7, with *btb* = 1,3,5-tris(4-carboxyphenyl)benzene. 150 mg of $\text{Bi}(\text{NO}_3)_3 \cdot 5\text{H}_2\text{O}$ (310 μmol) was mixed with 202 mg of the linker H_3btb (460 μmol) in 10 mL methanol in a 23 mL Teflon liner. To facilitate the deprotonation of the linker, 25 mg NaOH (620 μmol) was added to the reaction mixture. The mixture was ultrasonicated for 10 min. The Teflon liner was packed into a stainless-steel autoclave and heated at 120 °C for 12 h and subsequently cooled to room temperature. Afterwards, the obtained white powder was rinsed several times with methanol, subsequently sonicated in methanol for 30 min, and then activated in an oven at 160 °C for 12 h.

1.1.2. *SU-100*

Individual batches of *SU-100* were made by adding 20 mg $\text{Bi}(\text{NO}_3)_3 \cdot 5\text{H}_2\text{O}$ (50 μmol) and 15 mg biphenyl-3,4',5-tricarboxylic acid (52 μmol) into a 5 mL glass tube containing 3 mL of methanol. The tube was then sealed with a PTFE-lined polybutylene terephthalate cap and subsequently stirred and heated at 160 °C for 1 h using a pre-heated aluminum block, after which the white suspension was centrifuged at 8000 rpm for 10 minutes and left to dry overnight under ambient conditions. The described procedure was repeated, and the samples were pooled together in order to acquire larger quantities.

1.1.3. *Dense Bi(btc)*

Individual batches of *Bi(btc)* were made by adding 69.2 mg of freshly mortared $\text{Bi}(\text{NO}_3)_3 \cdot 5\text{H}_2\text{O}$ (175 μmol) and 30 mg benzene-1,3,5-tricarboxylic acid (143 μmol) into a 5 mL glass tube containing 3 mL of deionized water, which was then sealed with a PTFE-lined polybutylene terephthalate cap. The tube was heated to 150 °C in a pre-heated aluminum block while stirring for 5 minutes, after which the reaction was quenched by immersing the tube in cold water. The white suspension was centrifuged at 10000 rpm for 10 minutes, after which the acquired solid was washed with 20 mL of *N,N*-dimethylformamide, centrifuged again, and finally washed with 20 mL of deionized water. The described procedure was repeated and the samples were pooled together in order to acquire larger quantities.

1.1.4. *CAU-17*

Individual batches of *CAU-17* were made by adding 63 mg of freshly mortared $\text{Bi}(\text{NO}_3)_3 \cdot 5\text{H}_2\text{O}$ (160 μmol) and 31 mg benzene-1,3,5-tricarboxylic acid (147 μmol) into a 5 mL glass tube containing 3 mL of methanol, which was then sealed with a PTFE-lined polybutylene terephthalate cap. The tube was put into a pre-heated aluminum block where it was heated at 120 °C for 1 h while stirring. After quenching the reaction by putting the container in cold water, the white suspension obtained

was centrifuged at 8000 rpm for 10 minutes and left to dry overnight under ambient conditions. The described procedure was repeated and the samples were pooled together in order to acquire larger quantities.

1.1.5. SU-101

A room-temperature synthesis was carried out by adding 0.20 g ellagic acid (662 μmol) and 0.38 g bismuth acetate (984 μmol) into a mixture of 28 mL deionized water and 2 mL acetic acid. The suspension was then stirred for 48 hours before being centrifuged at 10000 rpm, after which it was left to dry overnight at 60 °C in air, resulting in a fine yellow powder.

1.1.6. BSG

Individual batches of bismuth subgallate were prepared by adding 47 mg of freshly mortared $\text{Bi}(\text{NO}_3)_3 \cdot 5\text{H}_2\text{O}$ (97 μmol) and 50 mg gallic acid monohydrate (266 μmol) to a 5 mL glass tube containing 3 mL of deionized water. The tube was then sealed using a PTFE-lined polybutylene terephthalate cap and put in a pre-heated aluminum block held at 180 °C, while stirring. After 1 hour, the tube was immersed in cold water, after which the solid was filtered off, washed with 20 mL of deionized water and 20 mL of ethanol and left to dry in air overnight.

1.2. Powder X-ray diffraction (PXRD)

1.2.1. Le Bail fitting

Powder X-ray diffraction (PXRD) data were collected on a Rigaku Smartlab X-ray diffractometer using Cu $K\alpha_1$ radiation ($\lambda = 1.54056 \text{ \AA}$) and a D/TEX Ultra 250 strip detector.

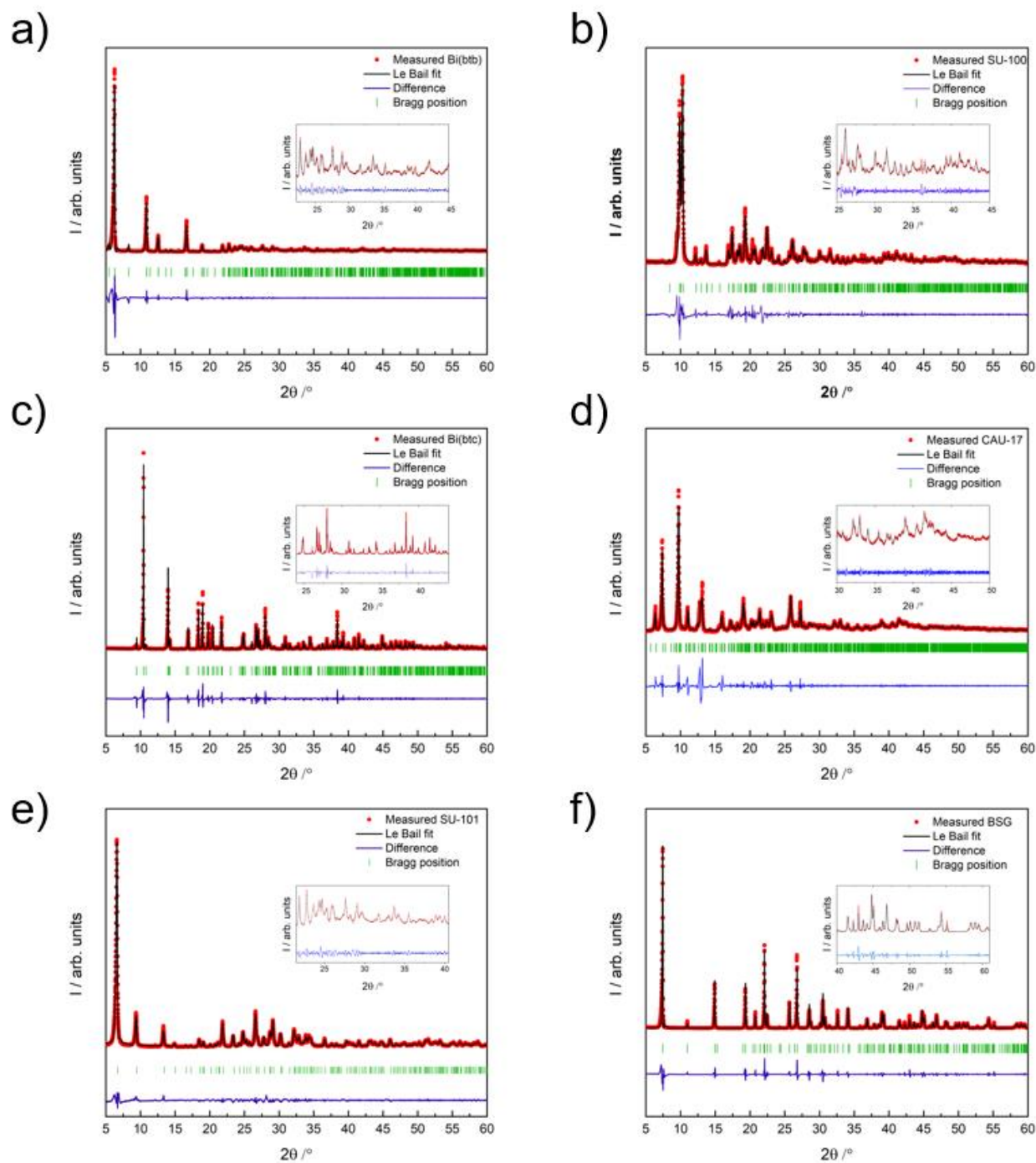


Fig. S1. Le Bail fits (black) to PXRD diffractograms collected on pristine CP powders (red) using known structural models: a) Bi(bt^b),² b) SU-100,³ c) Bi(bt^c), d) CAU-17,⁴ e) SU-101,⁵ f) BSG.⁶

Le Bail refinements were performed with a polynomial background and a Thompson-Cox-Hastings pseudo-Voigt function with axial divergence as the profile function.

Compound	Bi(btb)	SU-100	Bi(btc)	CAU-17	SU-101	BSG
Space group	<i>Pca2₁</i>	<i>I2/a</i>	<i>P2₁/c</i>	<i>P-3</i>	<i>P4₂/n</i>	<i>Pmna</i>
<i>a</i> / Å	32.370(6)	17.9264(4)	9.91385(8)	47.0594(18)	18.6404(1)	8.54028(8)
<i>b</i> / Å	3.1961(6)	9.7040(2)	16.93568(6)	47.0594(18)	18.6404(1)	4.66819(4)
<i>c</i> / Å	28.1423(9)	21.0311(9)	7.24707(6)	9.6928(4)	5.5559(1)	23.6962(1)
<i>α</i> / °	90	90	90	90	90	90
<i>β</i> / °	90	96.950(4)	70.5227(8)	90	90	90
<i>γ</i> / °	90	90	90	120	90	90
<i>V</i> / Å ³	3567.4(9)	3631.6(2)	1147.14(1)	18590(1)	1930.48(4)	944.71(1)
R_{Bragg} factor	1.57 · 10 ⁻²	7.27 · 10 ⁻³	2.24 · 10 ⁻²	0.246	7.10 · 10 ⁻³	1.97 · 10 ⁻²
R_F factor	1.72 · 10 ⁻¹	8.06 · 10 ⁻³	1.72 · 10 ⁻¹	0.151	1.91 · 10 ⁻²	6.71 · 10 ⁻²

Table S1: Le Bail refinement parameters.

1.2.2. CAU-17 stability

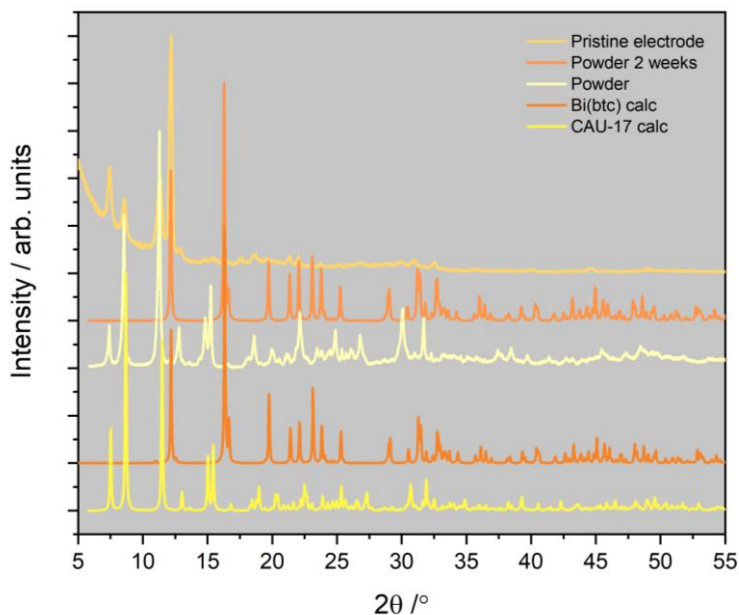


Fig. S2. Stability of CAU-17 investigated by powder diffraction. Data were collected using Co $K\alpha$ radiation ($\lambda=1.79 \text{ \AA}$) on the synthesized powder after drying (powder), after 2 weeks of shelf life as dry powder (powder 2 weeks), and after deposition as a film in Nafion ink on an electrode directly after drying (pristine electrode). These are compared to patterns calculated for dense Bi(btc) and CAU-17.⁴

Le Bail fitting verified that pristine CAU-17 was obtained during the synthesis (Fig. S1). After 2 weeks of storage at ambient conditions as a dry powder, the CAU-17 powder had converted into dense Bi(btc). However, CAU-17 was partly preserved when deposited as an ink on a glassy carbon electrode according to grazing incidence XRD (GI-XRD). For this electrode, two characteristic CAU-17 peaks below 10° are indicative of a large unit cell, while absence of the peak at 17° rules out dense Bi(btc). However, the diffraction pattern of the CAU-17 as deposited on the electrode somewhat differs from that of the pristine powder, as the two characteristic CAU-17 peaks around 16° are not present, and as the peak at 12° has shifted (e.g. due to changes in the solvent content in the pores). Nevertheless, in comparison with the pristine powder, CAU-17 is largely conserved in the Nafion ink. Consequently, it was possible to perform some electrochemical measurements on the material.

1.3. Extended X-ray absorption fine structure (EXAFS) - pristine powders

1.3.1. EXAFS analysis of Bi(btb)

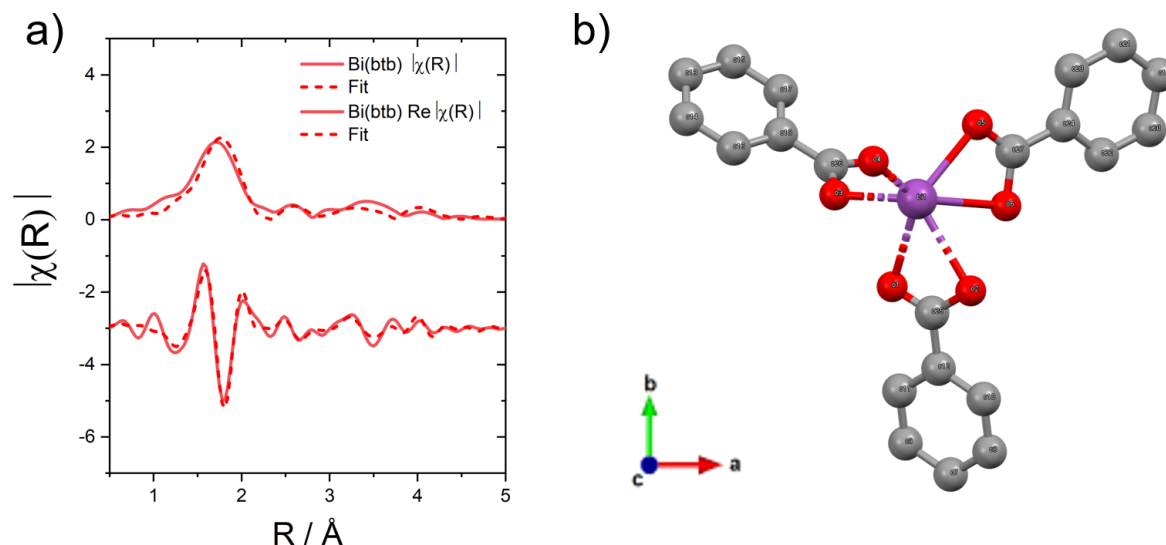


Fig. S3. a) EXAFS fit to Bi(btb) data based on a structural model.² b) Local coordination environment around Bi in the CP structure (Bi: purple, O: red, C: grey); the figure is generated using the VESTA software.⁷

Path	N	σ^2 (\AA^2)	ΔR (\AA)	R (\AA)
O3.1	3	0.008(2)	0.058(5)	2.196(5)
O2.1	3	0.020(5)	0.070(5)	2.295(5)
O1.2	1	0.011(6)	0.097(5)	3.695(5)
O2.2	1	0.011(6)	0.126(5)	4.835(5)
O3.2	1	0.011(6)	0.101(5)	3.847(5)
O4.2	1	0.011(6)	0.080(5)	3.051(5)
O5.2	1	0.011(6)	0.108(5)	4.147(5)
O6.2	1	0.011(6)	0.091(5)	3.473(5)
Bi1.1	2	0.012(7)	0.332(17)	4.248(17)
C18.1	3	0.006(9)	0.113(5)	4.307(5)
C24.1	1	0.006(9)	0.116(5)	4.448(5)
C12.1	2	0.006(9)	0.118(5)	4.518(5)
C16.1	1	0.006(9)	0.130(5)	4.976(5)
C22.1	1	0.006(9)	0.132(5)	5.054(5)
C24.2	1	0.006(9)	0.124(5)	4.764(5)
C12.2	1	0.006(9)	0.133(5)	5.087(5)

Table S2: Fitting parameters for Bi(btb). Single and double scattering paths are denoted .1 and .2, respectively. Additional refined parameters: $S_0^2 = 0.765 \pm 0.095$, $E_0 = 0.292 \pm 1.553$ eV. R-factor = 0.0507.

The number of nearest neighbors is determined to six oxygen atoms. It has previously been reported that Bi(btb) is nine-fold coordinated in BiO_9 clusters,² where three of the oxygen atoms coordinate to neighboring Bi atoms. Thus, our findings are in agreement with the published structure of Bi(btb).

1.3.2. EXAFS analysis of dense Bi(btc)

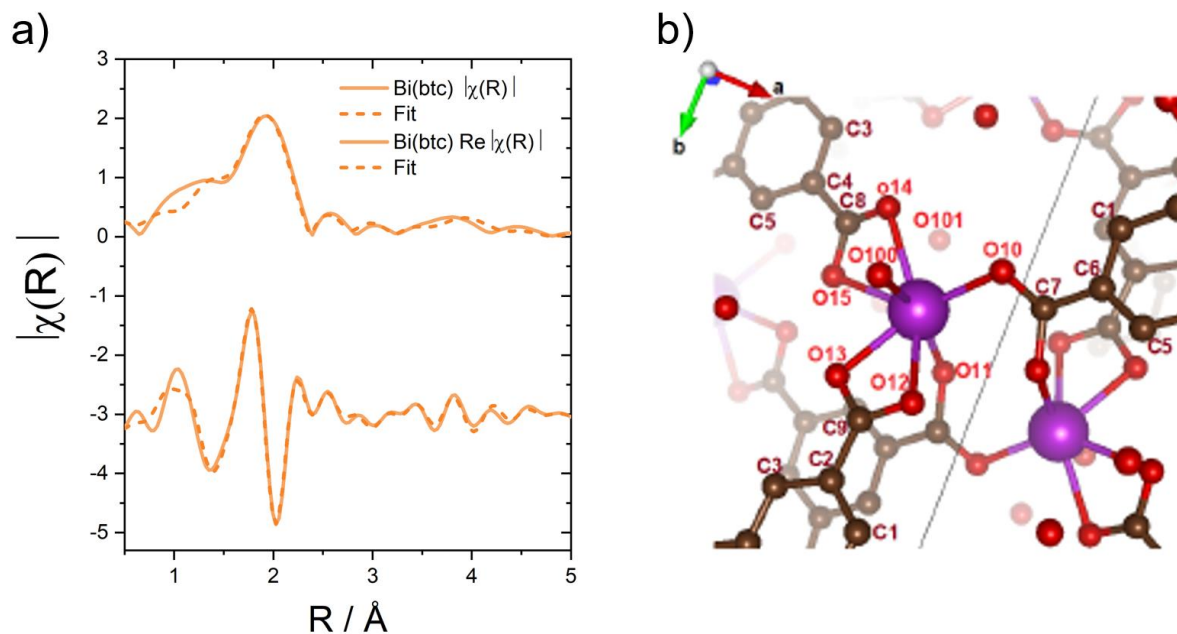


Fig. S4. a) EXAFS fit of dense Bi(btc) data based on a structural model. b) Local coordination environment around Bi in the CP structure (Bi: purple, O: red, C: brown) and atomic labels of the scattering atoms; the figure is generated using the VESTA software.⁷

Path	N	σ^2 (Å ²)	ΔR (Å)	R (Å)
O11.1	2	0.010(1)	-0.021(3)	2.201(3)
O13.1	6	0.010(5)	-0.023(3)	2.404(3)
O15.2	3	0.010(5)	-0.044(3)	4.685(3)
C2.1	3	0.005(4)	-0.142(3)	4.392(3)

Table S3: Fitting parameters for dense Bi(btc). Single and double scattering paths are denoted .1 and .2, respectively. Additional refined parameters: $S_0^2 = 0.925 \pm 0.077$, $E_0 = -5.667 \pm 0.793$ eV. R-factor = 0.0153.

The number of nearest neighbors was determined to eight oxygen atoms in agreement with the crystal structure. Further, this resembles the local coordination environment around Bi in CAU-17.⁴

1.3.3. EXAFS analysis of SU-101

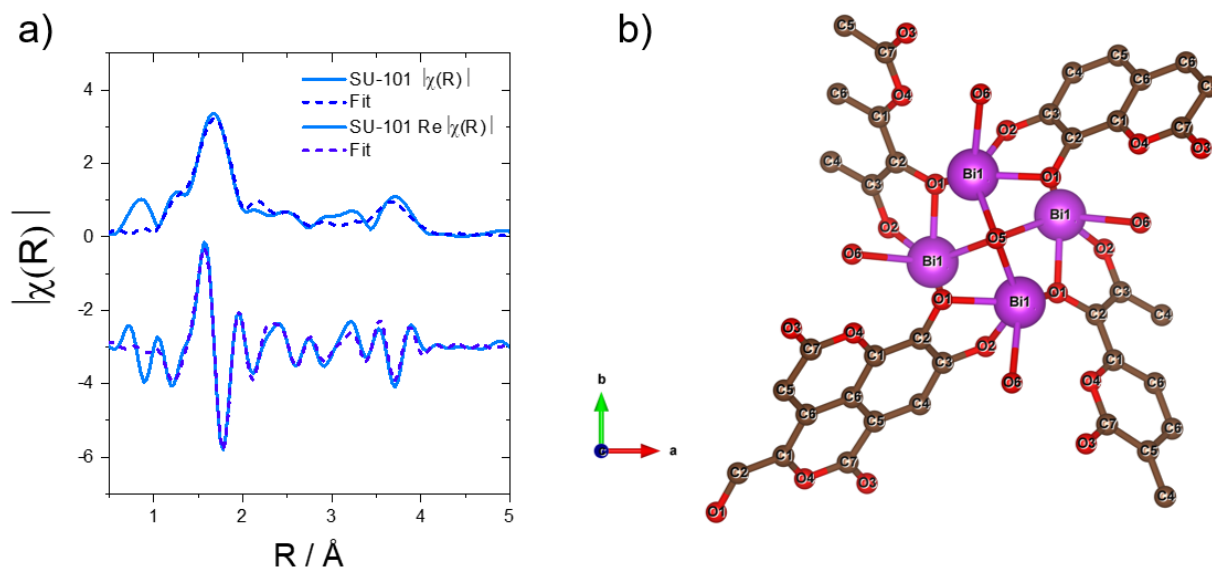


Fig. S5. a) EXAFS fit of SU-101 data based on a structural model.⁵ b) Local coordination environment around Bi in the CP structure (Bi: purple, O: red, C: brown) and atomic labels of the scattering atoms; the figure is generated using the VESTA software.⁷

Path	N	σ^2 (\AA^2)	ΔR (\AA)	R (\AA)
O6.1	4	0.006(1)	-0.062(4)	2.196(4)
O5.1	1	0.006(1)	-0.065(4)	2.295(4)
O4.2	2	0.009(1)	-0.069(4)	2.468(4)
O3.2	1	0.009(2)	-0.075(4)	2.652(4)
O6.2	2	0.009(2)	-0.083(4)	2.955(4)
O2.1	2	0.035(18)	-1.192(39)	1.873(39)
O5.2	1	0.009(2)	-0.085(4)	3.035(4)
Bi1.1	4	0.009(2)	-0.145(3)	3.812(3)

Table S4: Fitting parameters for SU-101. Single and double scattering paths are denoted .1 and .2, respectively. Additional refined parameters: $S_0^2 = 0.678 \pm 0.135$, $E_0 = 0.628 \pm 1.911$ eV. R-factor = 0.0285.

The number of nearest neighbors has been determined to five oxygen atoms. In literature, the coordination of Bi^{3+} is reported to be six-fold, with three bonds from the coordinating phenolates, two bridging μ_4 -oxygen atoms, and one terminally coordinated water molecule.⁵ From Fig. S5b only five short oxygen contacts are present around each Bi^{3+} , and thus we argue, our finding is in agreement with the published structure.

1.4. Scanning electron microscopy (SEM)

Scanning Electron Microscopy (SEM) images were acquired on a FEI-Nova Nano SEM 600.

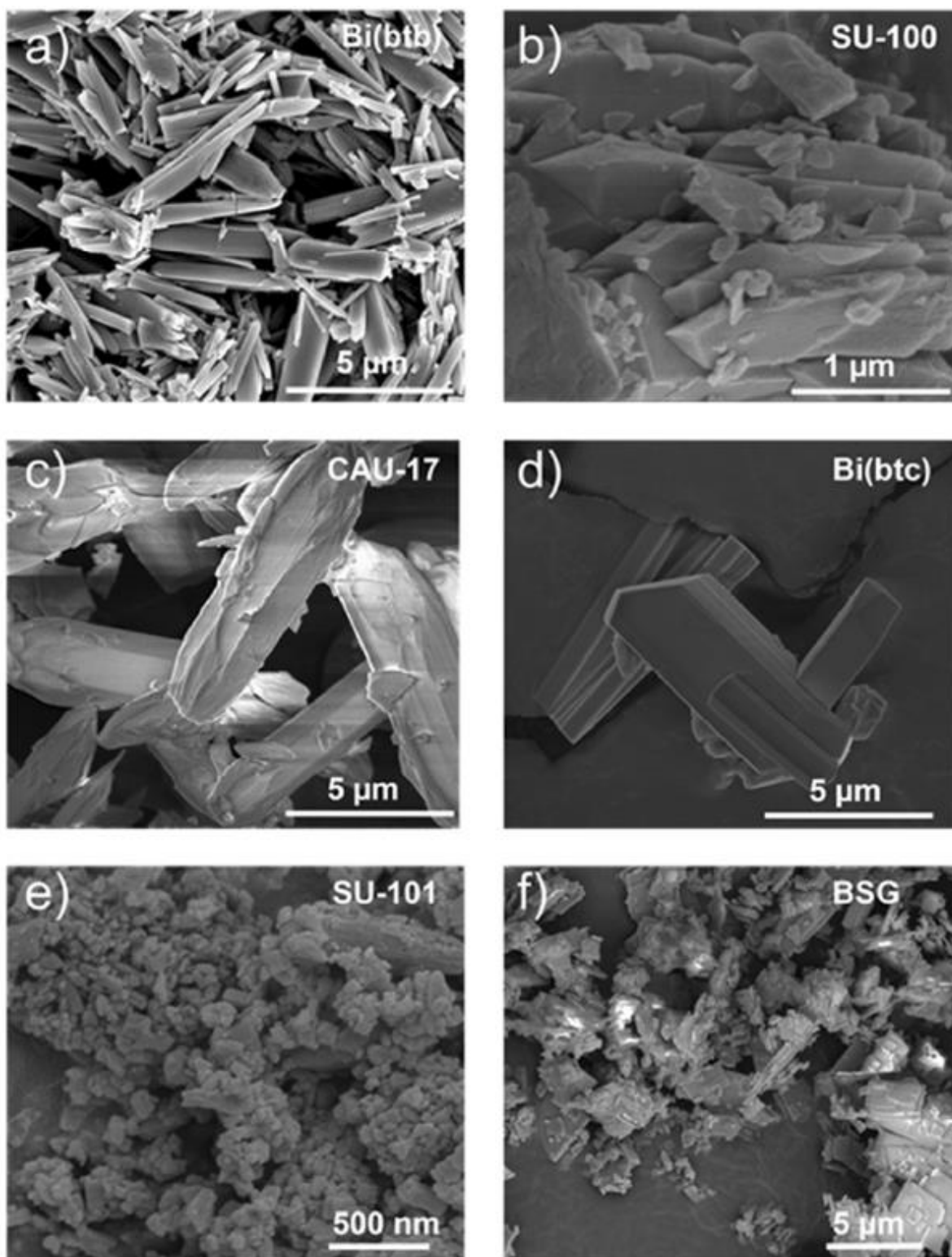
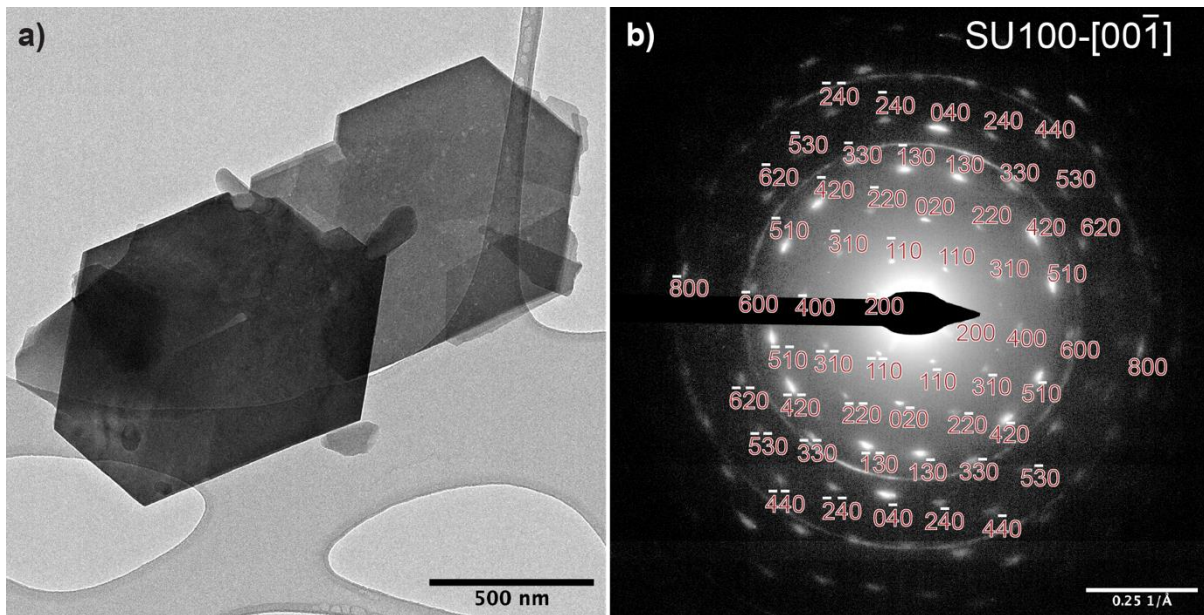


Fig. S6. SEM images of pristine CP powders coated with 7 nm Pt to limit charging effects. a) Bi(btb), b) SU-100, c) CAU-17, d) dense Bi(btc), e) SU-101, and f) BSG.

1.5. Transmission electron microscopy (TEM)



1.6. Void space analysis

Void space analysis was performed using Crystal Explorer 3.1 and crystallographic information files (CIF) with an isovalue of $0.002 \text{ e} \cdot \text{au}^{-3}$,⁸ and the standard void cluster equal to the unit cell +5 Å. All solvent molecules were removed from the structures prior to performing the calculations.

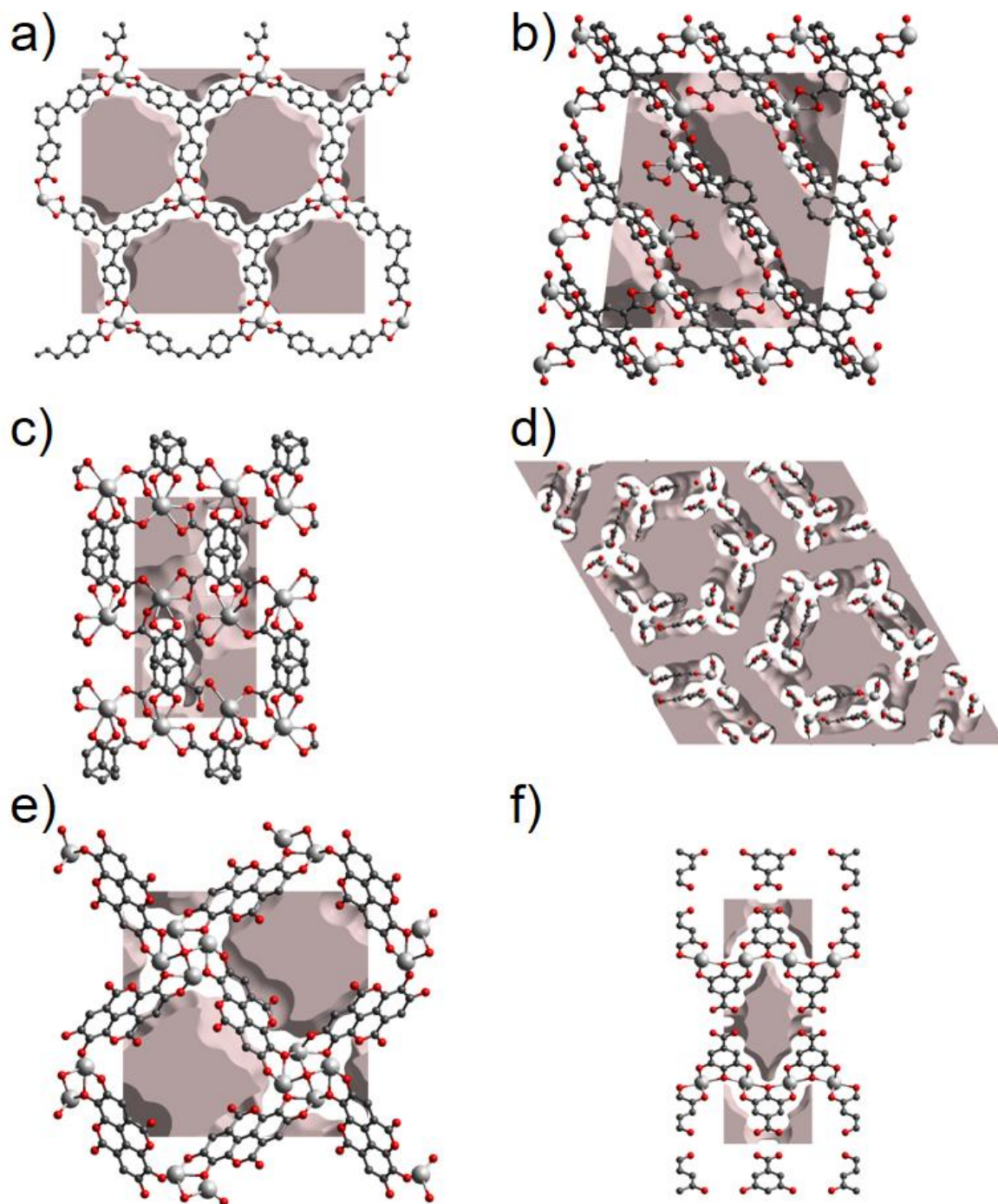


Fig. S8. Crystal void space of a) *Bi(btb)*,² b) *SU-100*,³ c) *Bi(btc)*, d) *CAU-17*,⁴ e) *SU-101*,⁵ and f) *BSG*.⁶

1.7. Thermogravimetric analysis (TGA) and differential scanning calorimetry (DSC)

The combination of TGA and DSC allows for monitoring mass changes while analyzing phase transitions. Thermogravimetric analysis data were recorded on a NETZSH TG 209 F1 Libra TGA instrument. DSC was recorded on a NETZSH DSC 401 F1 Pegasus instrument.

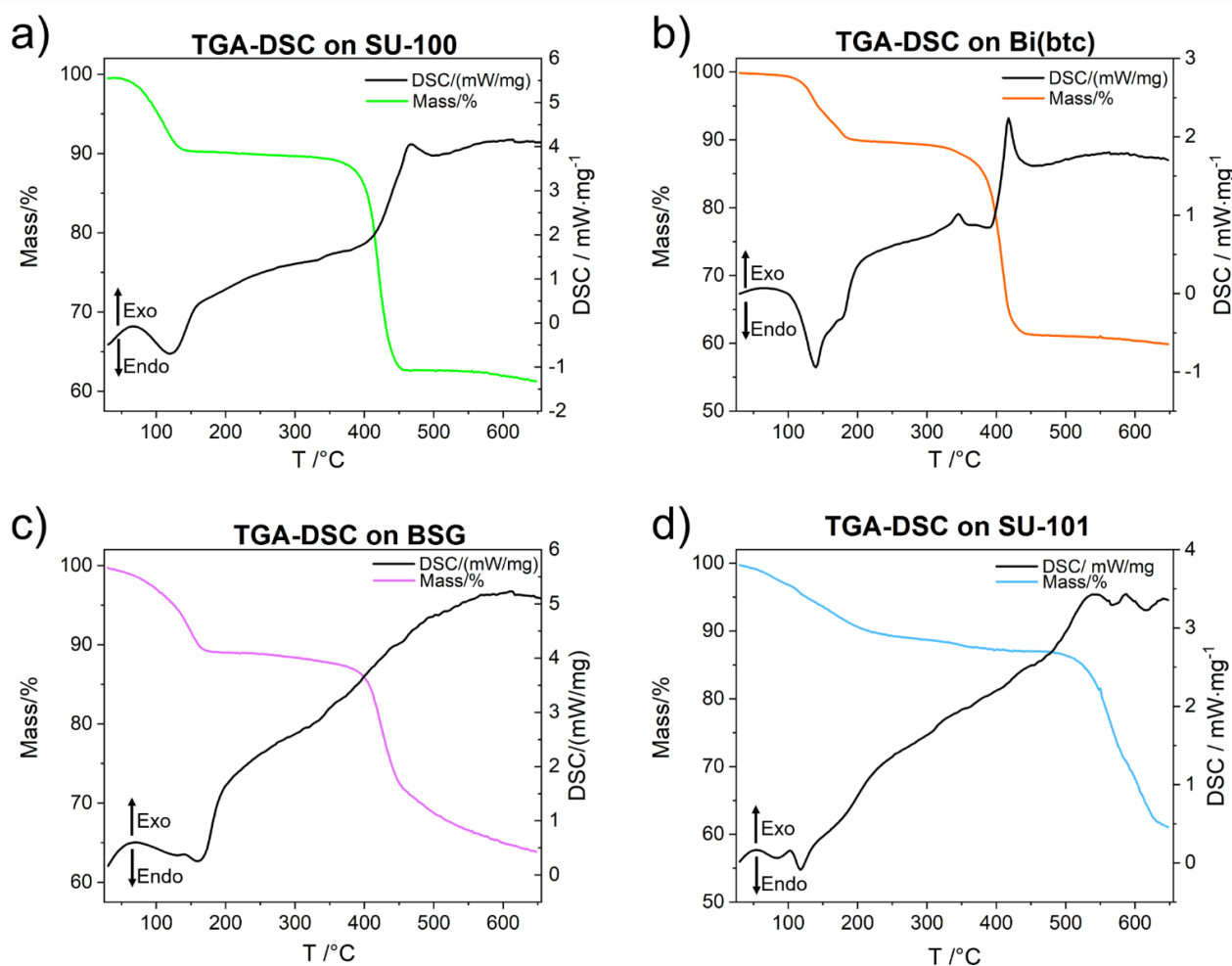


Fig. S9: Combined TGA and DSC measured in N₂ atmosphere on a) SU-100, b) Bi(btc), c) BSG, and d) SU-101. Arrows indicate the endo- and exothermic directions of heat transfer.

We attribute the thermal transition at approx. 100 °C to loss of solvent molecules from the structures. Due the large temperature interval of this transition, the mass loss is investigated in larger detail in Fig. S10.

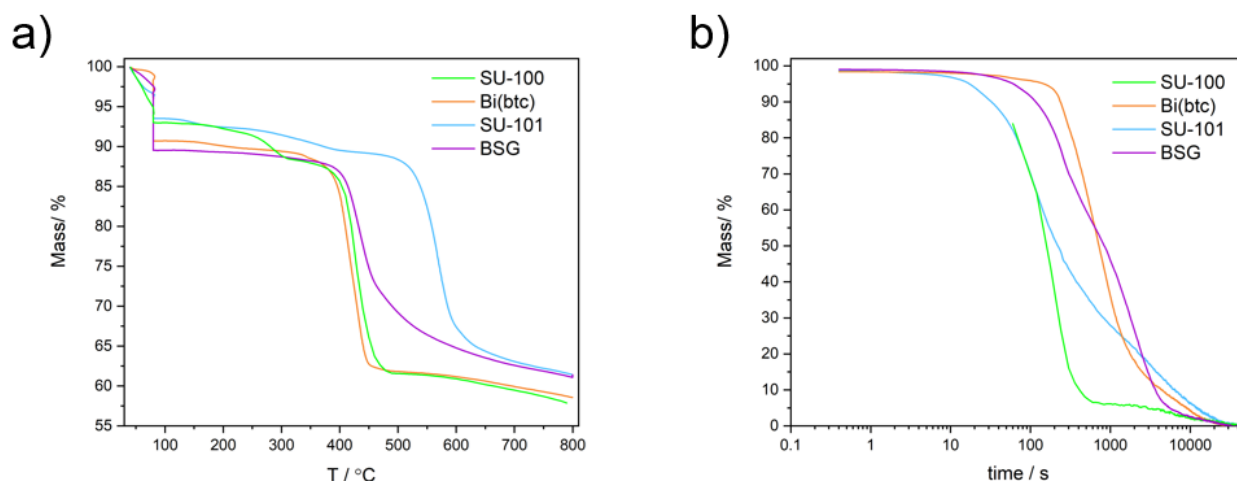


Fig. S10. TGA in N_2 atmosphere on SU-100, Bi(btc), SU-101, and BSG. The temperature 80 °C was held for 12 h ($43 \cdot 10^3$ s). a) Full TGA curves and b) mass as a function of time for the isothermal treatment at 80 °C. In figure a) the mass of the sample is normalized with respect to the total sample mass, while in figure b) it is normalized with respect to the mass loss during the isothermal treatment.

Fig. S10a and S10b report the TGA results from a three-segment method (heating-isotherm-heating). The samples were: 1) heated at $10 \text{ }^\circ\text{C} \cdot \text{min}^{-1}$ from room temperature to 80 °C, 2) kept at 80 °C for 12 hours to allow for solvent removal, and 3) heated at $10 \text{ }^\circ\text{C} \cdot \text{min}^{-1}$ to 800 °C. The mass versus temperature and the isothermal segment in terms of mass versus time are reported in Fig. S10a and S10b, respectively.

From Fig. S10a it is evident that the primary thermal transitions of the samples are in line with the measurements shown in Fig. S9 and reported in Table 1 in the manuscript, i.e. the mass loss observed below approx. 150 °C in Fig. S9 can be ascribed to solvent loss. However, from these measurements it is also clear that the samples SU-100 and SU-101 have a thermal transition around 250 °C and 230 °C, respectively. This latter mass loss was less evident in the one-segment TGA reported in Fig. S9. We suggest the transition around 230 °C/250 °C might be due to partial decomposition of the organic linker.

From Fig. S10b we conclude that the isothermal treatment at 80 °C allows for the removal of all solvent present in the samples, since the mass stabilizes within the 12 h at 80 °C. The kinetics of solvent desorption show very different time constants, τ , with $\tau_{\text{SU-100}} < \tau_{\text{SU-101}} < \tau_{\text{Bi(btc)}} \sim \tau_{\text{BSG}}$. The desorption kinetics are in line with the experimental measurement of the sample porosity (Table 1 in the manuscript) with SU-100 as the sample with the highest open porosity (exposed surface area) followed by SU-101, Bi(btc) and BSG. From the analysis of the isotherms, we also observe that SU-101 is characterized by two different time constants: one similar to the SU-100 sample (short-time) and one representative of a dense material (long-time). This feature suggests that in SU-101 porous and dense domains might coexist.

2. Electrochemical characterization

2.1. Cyclic voltammetry (CV)

Cyclic voltammetry was performed in saturated Ar and CO₂ atmosphere, recorded using a CHI-660-E potentiostat.

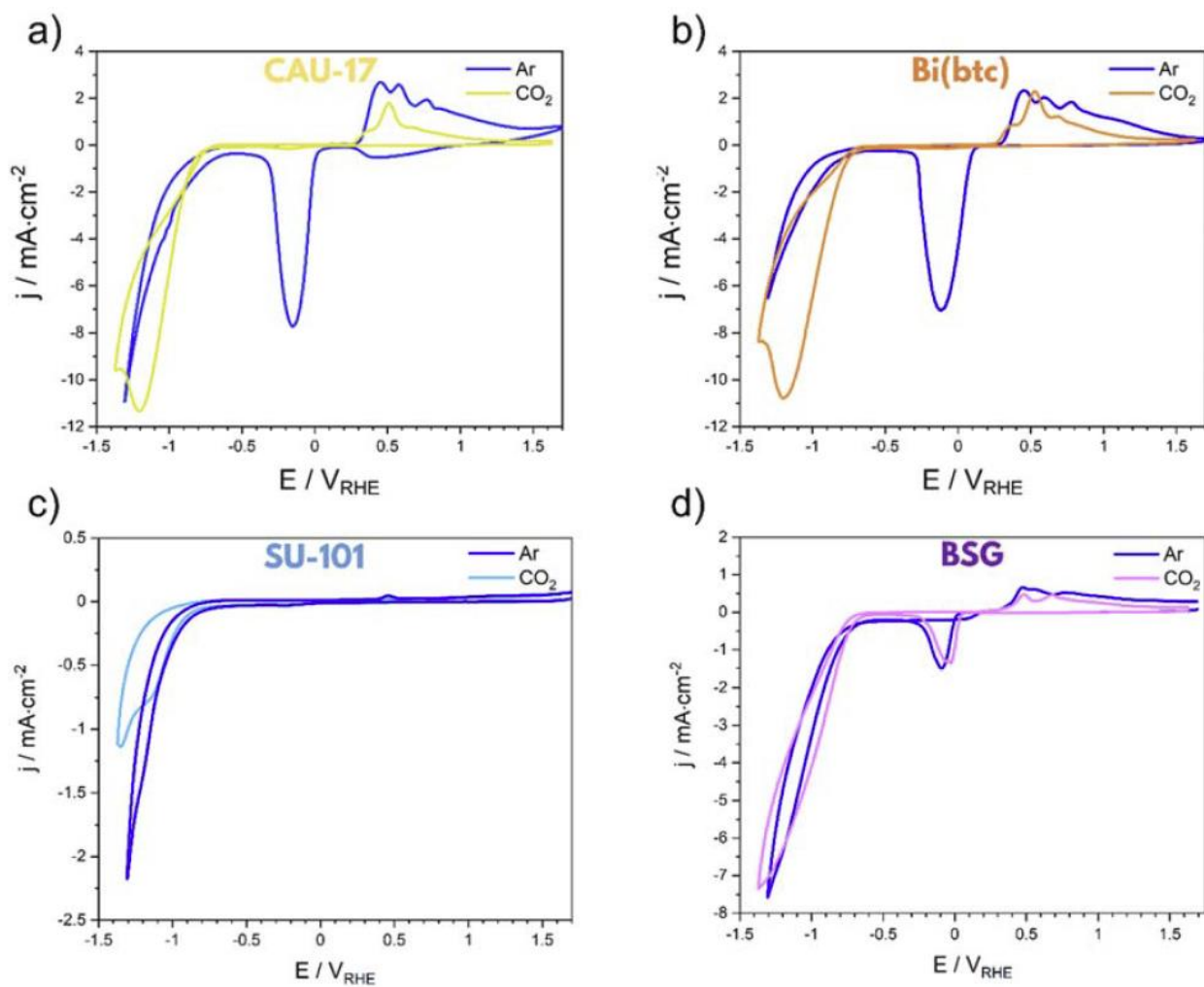


Fig. S11. Cyclic voltammograms recorded on a) CAU-17, b) dense Bi(btc), c) SU-101, and d) BSG, at 50 mV·s⁻¹ in Ar and CO₂ saturated 0.5 M KHCO₃ (aq).

2.2. Reduction peak of bismuth

From the cyclic voltammograms, the maximum current recorded at the reduction peak of Bi(III)→Bi(0) has been normalized to the bismuth content and plotted across the six CPs. It is hypothesized that the size of the reduction peak in Ar is a measure of the redox stability of Bi in the CP structure. Hence, a large reduction peak represents an easy conversion of Bi(III) in the CP to Bi(0) species.

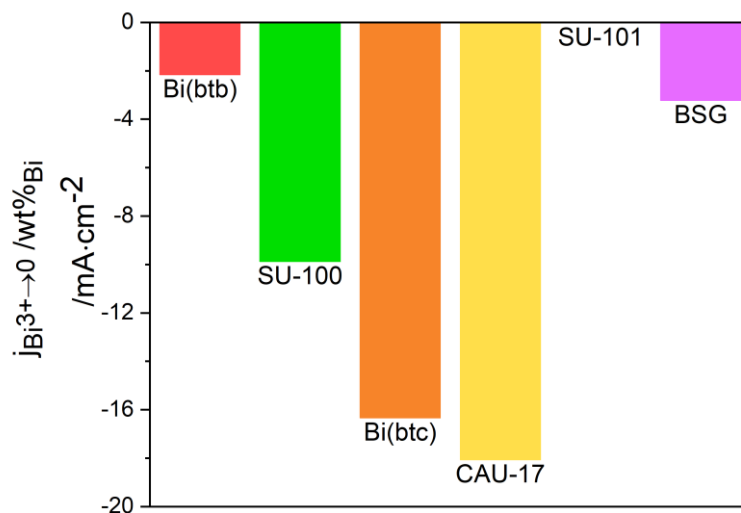


Fig. S12. Maximum current density at the reduction peaks for $Bi^{3+} \rightarrow Bi^0$ in Ar saturated $KHCO_3$ (aq) electrolyte normalized to the weight fraction of bismuth in the CP. Data for Bi(btb) is from our previous study and has been included for comparison.¹

2.3. Bulk electrolysis

Bulk electrolysis was recorded on a CHI-660-E potentiostat.

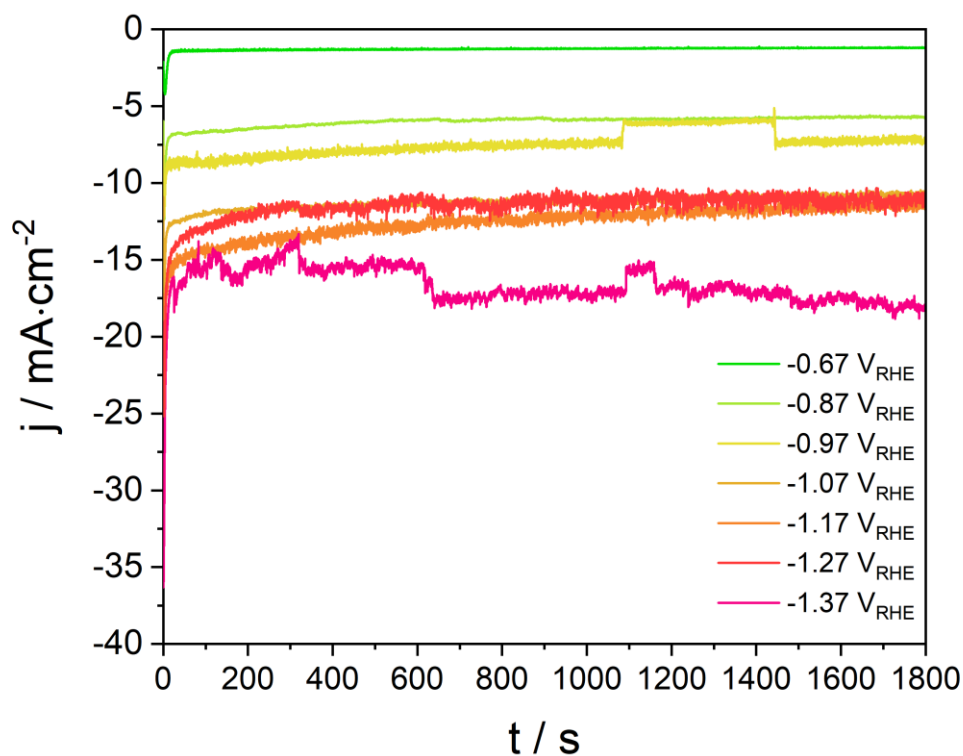


Fig. S13. Representative chronoamperometric responses of SU-100 at different applied potentials in CO_2 -saturated KHCO_3 (aq). The abrupt jump in current seen at $-0.97 V_{\text{RHE}}$ is due to a sudden movement of electrodes, whereas the increase in noise at more negative potentials is due to generation of bubbles at the electrode surface due to the hydrogen evolution reaction (HER).

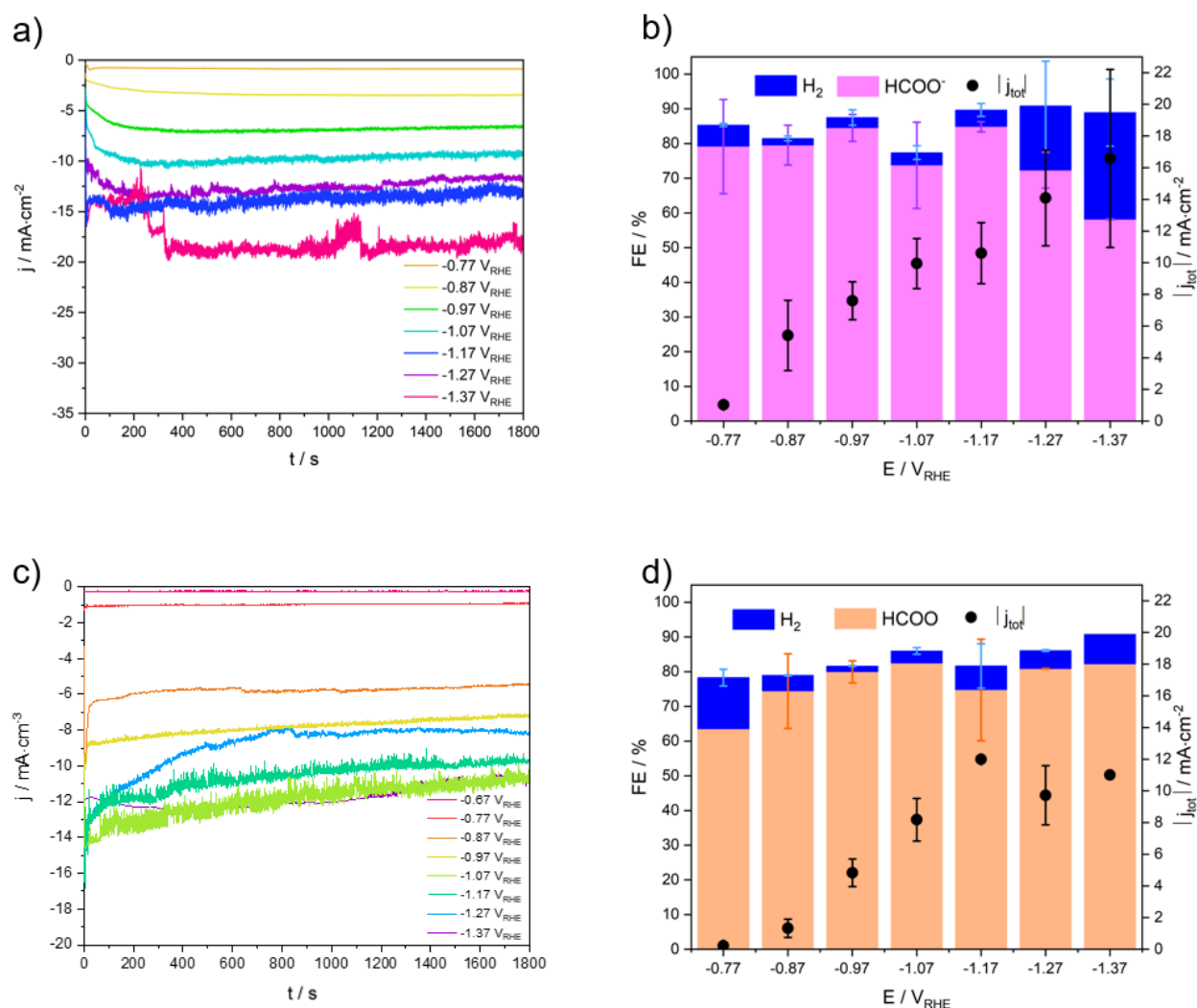


Fig. S14. Bulk electrolysis on BSG (a and b) and dense Bi(btc) (c and d). a) Representative chronoamperometric responses of BSG. A linear increase in activity is observed within the first 200 s corresponding to an activation of the material, afterwards the current stabilizes. b) Current density and selectivity after 30 min of electrolysis on BSG. c) Chronoamperometry on dense Bi(btc). d) Current density and selectivity after 30 min of electrolysis on Bi(btc); the maximum current is obtained at -1.17 V_{RHE}.

The presence of a mass-limited regime is corroborated by the fact that all the materials have a similar current density when the plateau region is reached. Indeed, if the diffusion of CO₂ is the limiting factor, the current density must be similar since it depends upon the boundary layer thickness close to the electrode. Thus, the plateau current depends on the electrochemical cell geometry and stirring rate (which were kept constant during the experiments) and not on the activity of the catalysts.

For dense Bi(btc), we do not observe a further increase in current density at more reducing potentials than -1.17 V_{RHE} i.e. after having reached the CO₂ limiting flux. We speculate that this is due to the nature of the sample (see Fig. S18b), where the bulky CO₂ molecules potentially could be trapped in the small pores which will limit the HER as well.

2.4. Overpotentials

Overpotentials have been determined, given that the equilibrium CO_2 -to-formate potential is $-0.20 \text{ V}_{\text{RHE}}$. The $\text{Bi}(\text{btb})^*$ value is from our previous study.¹ The onset potentials reported from cyclic voltammetry: Onset (CV) is determined as the intersection between a baseline and a tangent to the steepest point of the CV curve. The onset potential from bulk electrolysis: Onset (it) is found as the intersection of the tangent at $E_{1/2}$ with the potential axis.

Sample	$\text{Bi}(\text{btb})^*$	SU-100	$\text{Bi}(\text{btc})$	CAU-17	SU-101	BSG
Onset (CV) / V_{RHE}	-	-0.83	-0.80	-0.87	-0.94	-0.74
$\eta(\text{CV}) / \text{mV}$	570	630	600	670	740	540
Onset (it) / V_{RHE}	-	-1.25	-1.45	-	-	-1.35
$\eta(\text{it}) / \text{mV}$	-	420	620	-	-	520

Table S5: Comparison of the overpotentials for the CO_2 -to-formate conversion for the different CPs.

2.5. Bulk electrolysis for 1 h and 2 h

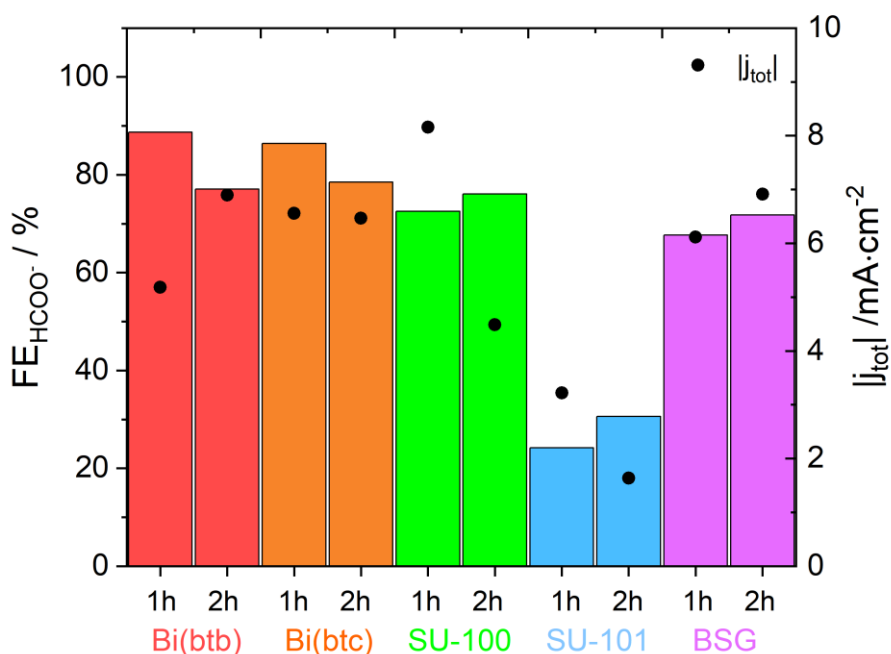


Fig. S15. Bulk electrolysis at $-0.97 \text{ V}_{\text{RHE}}$ for five CPs for 1 h and 2 h. The electrolyte was saturated with CO_2 prior to the experiment. Experiments were performed in a glass frit cell; thus, the selectivity is expected to be slightly lower than for the Nafion membrane cell used for the full screens (Fig. 3 and S14). The experiments were only performed once, and only trends can be inferred. However, the selectivity between 1 and 2 h are conserved within the errors from the full screens (Fig. 3 and S14) and comparable current densities are observed.

3. Structural changes during electrocatalysis

3.1. Scanning electron microscopy (SEM)

3.1.1. Investigation of the electrode preparation process

The effect of small modifications in the electrode preparation process was investigated for SU-100 and Bi(btb) in Fig. S16 and S17. The fibre formation observed after drying the ink in an oven (Fig. S16a) does not appear in a similar pristine SU-100 electrode exposed to slower drying in isopropanol (iPrOH) atmosphere at room temperature (Fig. S16b). Further, significant morphology changes are observed when comparing electroreduced Bi(btb) and SU-100 exposed to different drying processes (Fig. S16c-d and S17c-d). While these observations suggest that the microstructure of the active electrode materials may depend on small differences in the electrode preparation, it was beyond the scope of this study to investigate this aspect in more detail. However, in this study the electrodes were dried in an oven at 50 °C for 1 h.

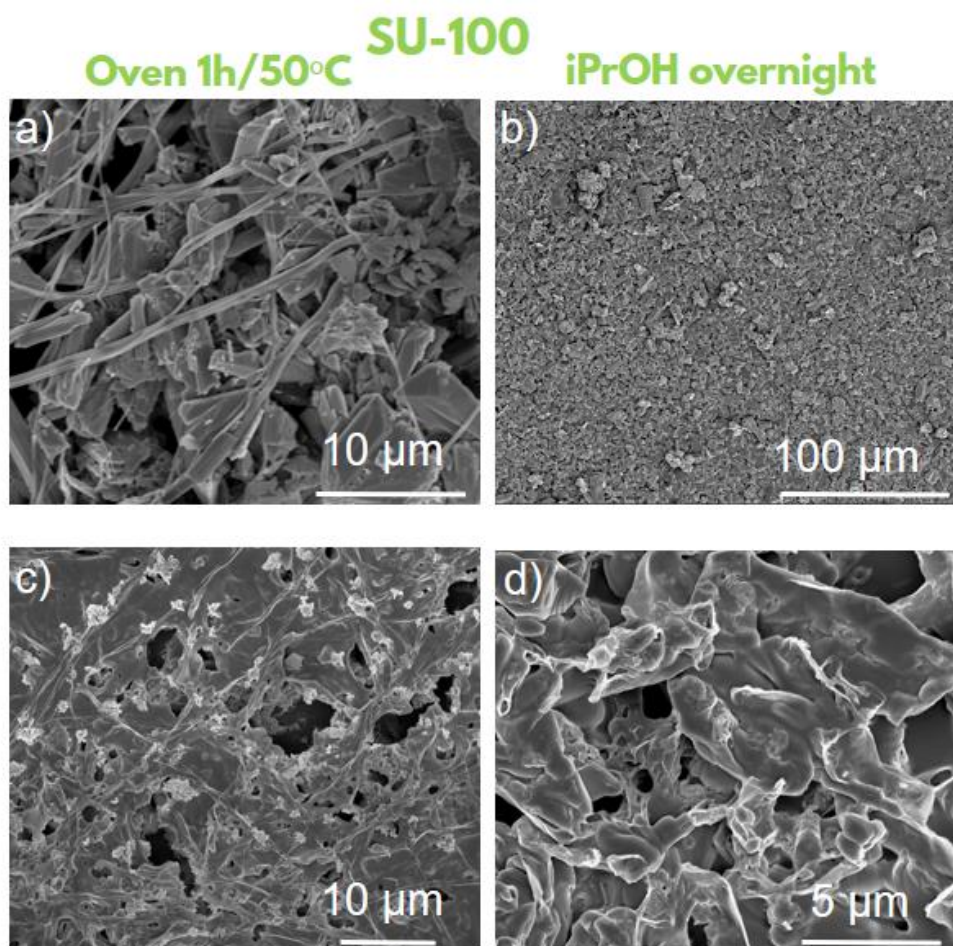


Fig. S16. SU-100 film prepared by drying in an oven for 1 h at 50 °C (a and c) and in iPrOH atmosphere overnight (b and d) as in our previous study.¹ a)-b) pristine electrodes, and c)-d) electroreduced electrodes at $-0.97 V_{RHE}$ for 30 min in CO_2 saturated $KHCO_3$ (aq) electrolyte.

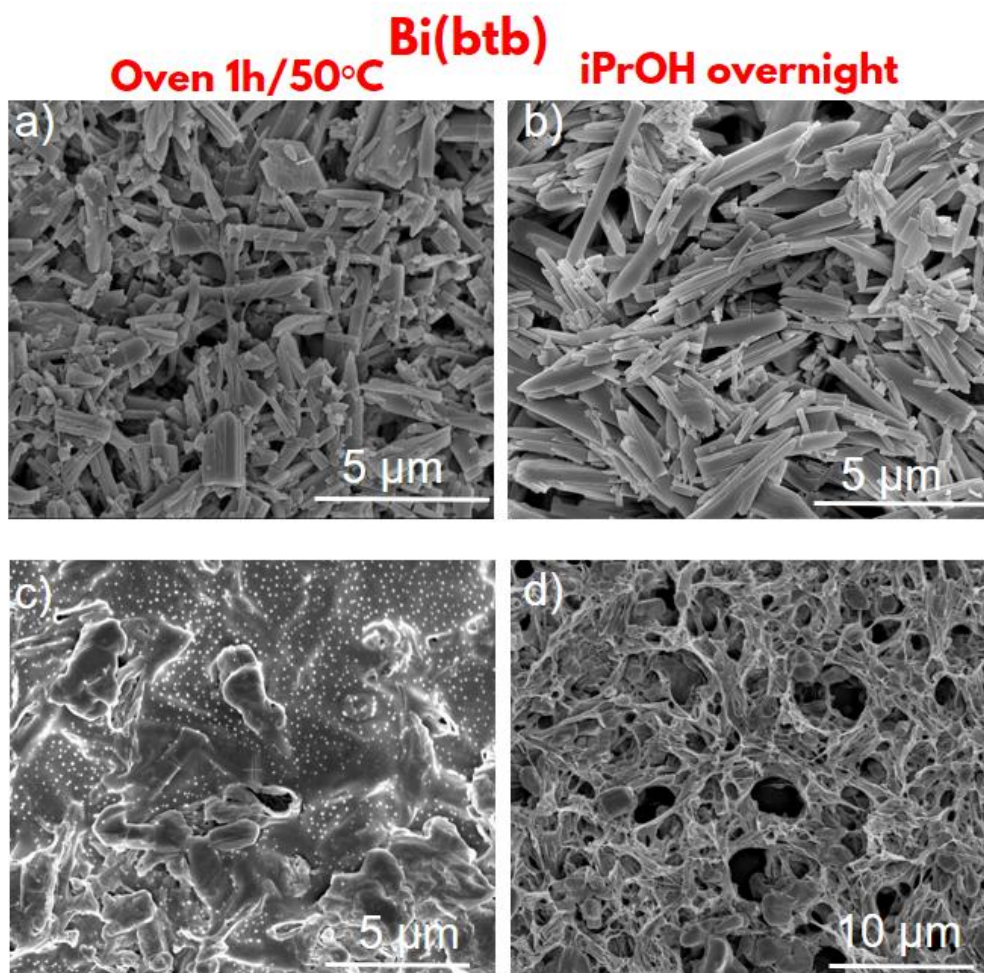


Fig. S17. Bi(bt_b) film prepared by drying in an oven for 1 h at 50 °C (a and c) and in iPrOH atmosphere overnight (b and d) as in our previous study.¹ a)-b) pristine electrodes, and c)-d) electroreduced electrodes at -0.97 V_{RHE} for 30 min in CO₂ saturated KHCO₃ (aq) electrolyte.

3.1.2. Pristine and reduced coordination polymer electrodes

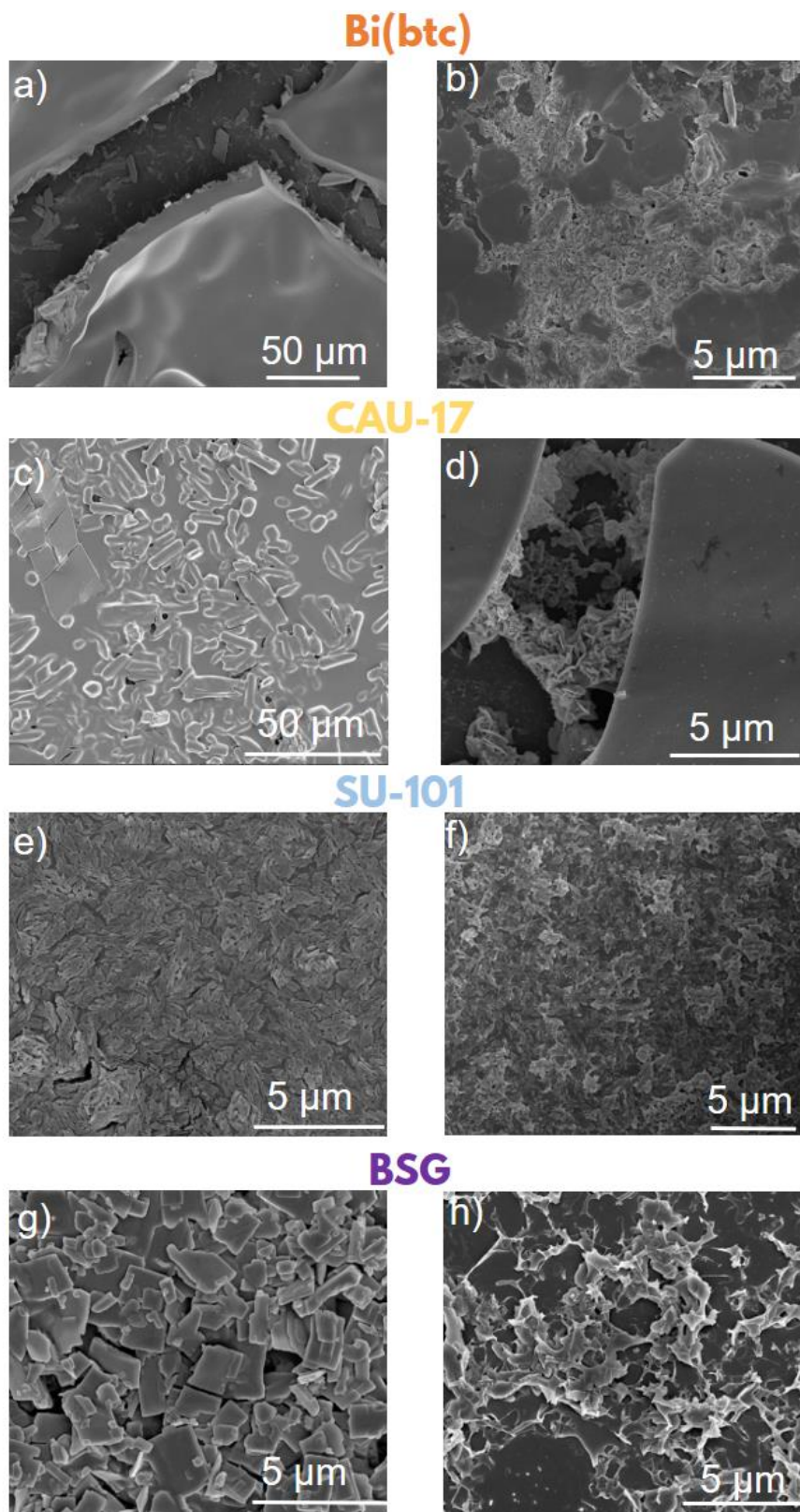


Fig. S18. SEM images of oven-prepared electrodes: a), c), e), and g) pristine, and b), d), f), and h) electroreduced for 30 min at $-0.97 V_{RHE}$ in CO_2 saturated $KHCO_3$ (aq) electrolyte.

The smooth surface seen in Fig. S18a-d is most likely the Nafion creating a layer on top of the particles. In Fig. S18a,c, Bi(btc) and CAU-17 particles, respectively, are seen underneath the Nafion film. Due to the density of the CP particles, they deposit below the Nafion. This suggests that the CP itself is in better electrical contact with the electrode, which allows for a more efficient charge transfer. The limitation for charge transfer would then be expected to be mass diffusion of CO_2 through the pores of Nafion, but CO_2 can reach the catalysts *via* the visible cracks in the surface.

3.2. Soaking in the electrolyte KHCO_3

3.2.1. Scanning electron microscopy

SU-100, soaked

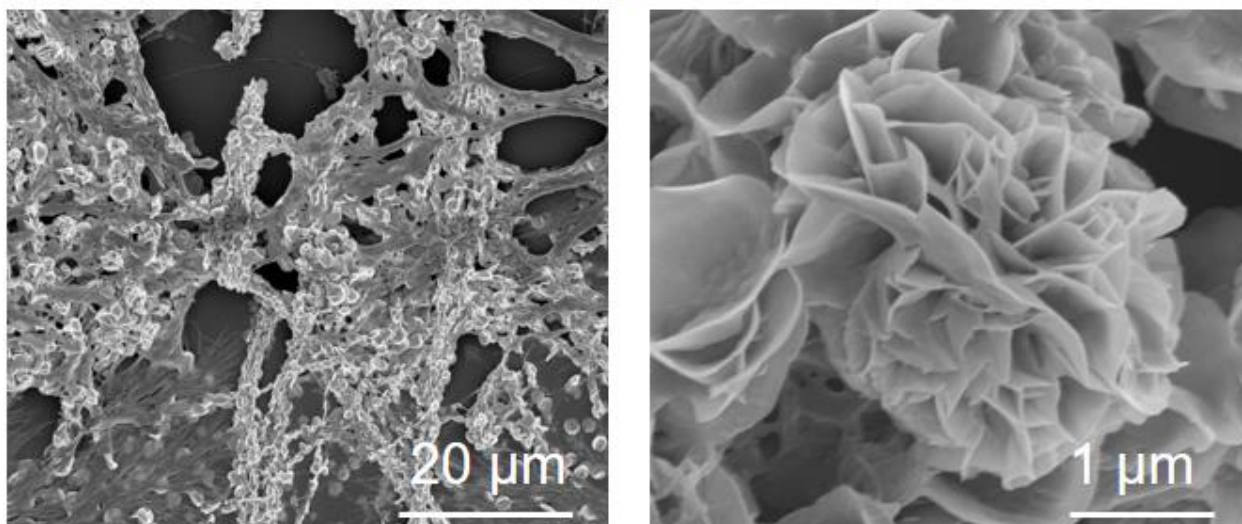


Fig. S19. SU-100 film soaked in 0.5 M KHCO_3 (aq) electrolyte for 15 min.

3.2.2. Powder X-ray diffraction (PXRD)

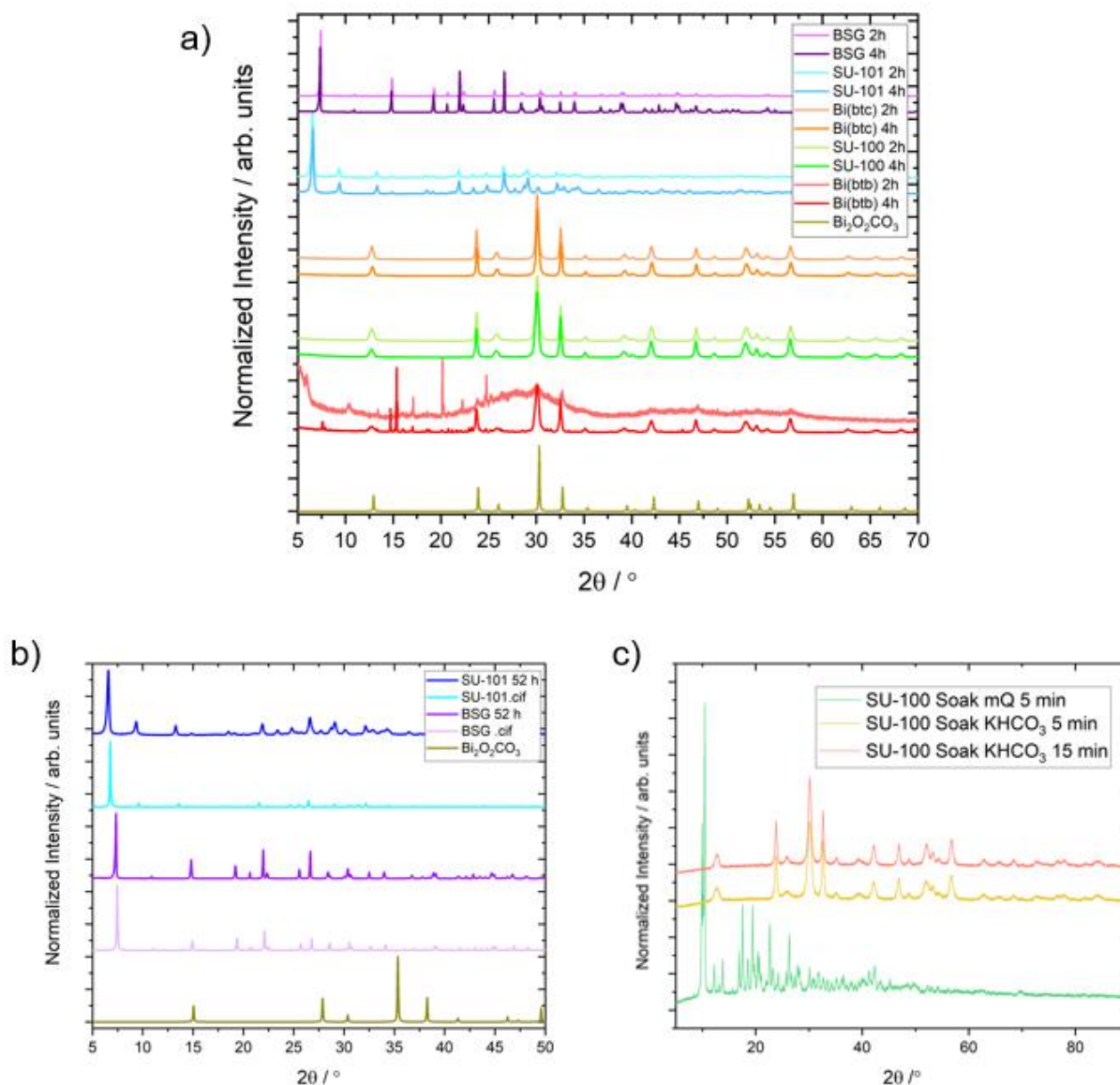


Fig. S20. a) PXRD data of powders soaked in 0.5 M KHCO₃ (aq) for 2 and 4 hours. For BSG and SU-101 it is evident that the structures are conserved even after 4 hours of soaking in the electrolyte. SU-100 and Bi(btc) are converted within the first two hours to a phase corresponding to Bi₂O₂CO₃.⁹ Bi(btb) has a longer stability in the electrolyte, but changes gradually. The calculated pattern of Bi₂O₂CO₃ is shown for comparison. b) The stability of SU-101 and BSG in the electrolyte for 52 hours. A comparison with the calculated diffractograms shows that the materials are stable in the electrolyte. The experimental patterns are shown in bright blue and bright purple. c) PXRD patterns demonstrating that SU-100 is converted to the Bi₂O₂CO₃ phase within the first 5 min. A blank test in milliQ (mQ) water shows, it is not the soaking in water that introduces the structural changes.

3.3. Transmission electron microscopy (TEM)

3.3.1. Additional information on HR-TEM and scanning nanobeam diffraction experiments

The Talos FX-200 microscope is equipped with a Ceta 16M camera with samples mounted in a double tilt holder. A 100 μm object aperture was used during imaging. Fast Fourier transforms (FFT) of high resolution TEM images were calculated using HyperSpy,¹⁰ the images were apodized using a Hann window prior to FFT. The resulting power spectra of the FFTs are displayed on a log scale with the minimum value to display set at the 30th percentile. Selected area electron diffraction patterns were collected on the same Ceta 16M camera on the same microscope.

Scanning electron nanobeam diffraction (SEND) experiments were performed with the microscope in microbeam mode and equipped with a 20 μm probe forming C2 aperture, thus effectively providing a convergence angle of 0.6mrad. Data was again collected on the Ceta 16M camera, albeit binned to 256x256 and in high dose mode. The dwell time at each probe position was 250 ms to ensure good signal-to-noise ratio. Some minor drift was observed during data collection, however, the relatively low spatial resolution chosen, and the large probe dimensions render this small amount of drift practically insignificant. The broad streaking observed in some diffraction patterns is due to insufficient detector corrections.

3.3.2. STEM-EDX data analysis

The EDX data were analysed in several ways. The intensities of individual spectral lines were mapped out after a background correction, which involved linear interpolation between (manually) selected areas without any peaks on each side of the spectral peak in question. The maps showing a quantified elemental composition as a function of probe position are obtained by using the Cliff-Lorimer k-factor method to quantify the local composition at each given probe position and map it out. The k-factors used are the ones provided by the manufacturer and have not been further calibrated, thus increasing the quantitative uncertainties somewhat. Thickness dependent absorption correction was applied, based on thickness estimates from correlation of HAADF image intensity and known platelet thickness. The displayed quantified elemental maps were filtered using a gaussian filter with a sigma value of 1.5 pixel. The quantified maps showed some single- or 2-pixel spikes in “vacuum” areas of the sample. These unavoidable spikes were removed by multiplying the quantified map with a binary mask. The mask was obtained by thresholding of the HAADF image followed by dilation of a 3-pixel kernel. This masking ensured that only areas with actual sample present are shown, which leads to a better use of the entire range of the colormap chosen for visualization. The same masks were also used for the Bi/O ratio maps. The quoted average Bi/O ratio was determined by fitting the summed spectrum of all probe positions in a given scan to give the best signal-to-noise ratio. The summed spectrum was fitted using the fitting routines implemented in HyperSpy, involving a thickness correction, a polynomial background function and inclusion of both major and minor elemental lines. The determined compositions of Bi and O, respectively, were determined once again using the Cliff-Lorimer approach and their extracted major line intensities, *i.e.* Bi-L α and O-K α .

3.3.3. Soaked SU-100 powder

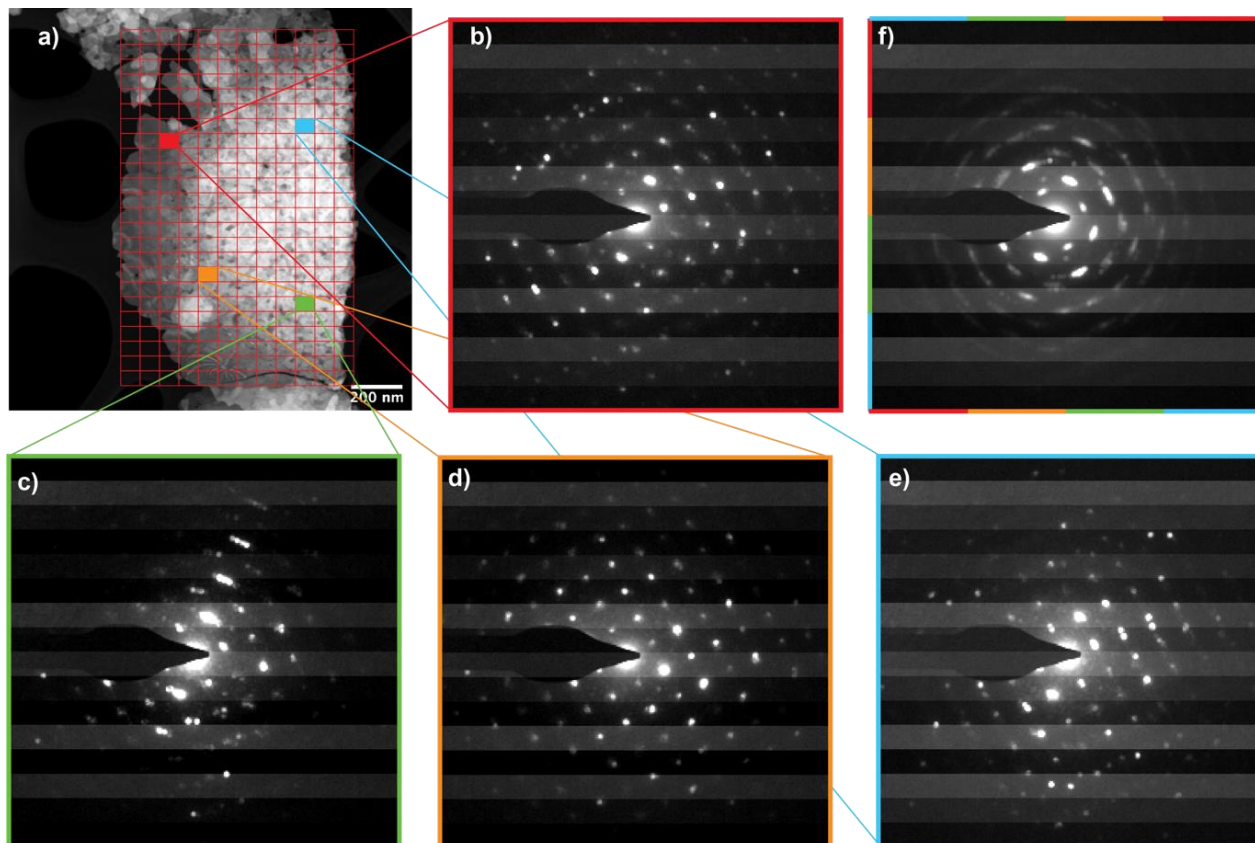


Fig. S21. TEM investigations of SU-100 powder soaked in KHCO_3 (aq) electrolyte. a) HAADF-STEM image with a grid overlaid to illustrate the scanning pattern employed for scanning electron nanobeam diffraction (SEND). The filled squares refer to selected probe positions from which the respective SEND patterns are shown in b)-e). In b) and c) there seem to be satellite reflections in several directions for many of the parent reflections, while in e) there are indications of twinning, f) is a sum of all 288 patterns. Clearly, the structure inspected is highly complex.

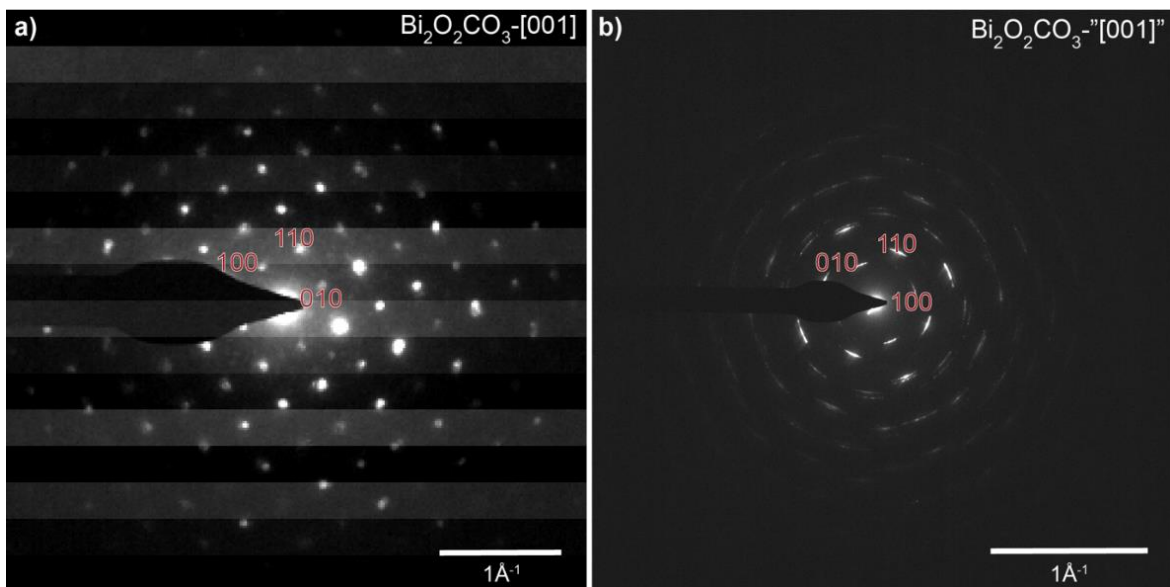


Fig. S22. TEM investigations of SU-100 powder soaked in KHCO_3 (aq) electrolyte. a) The pattern in Fig. S21d) is shown here and indexed according to the $[001]$ zone-axis pattern of the $\text{Bi}_2\text{O}_2\text{CO}_3$ phase. b) is a SAED pattern of the entire region and, as expected, looks very similar to the sum of all SEND patterns. Upon inspection of the individual patterns, the sum of all SEND patterns and the SAED pattern, it is clear that the micrometer sized area investigated consists of $\text{Bi}_2\text{O}_2\text{CO}_3$. Interestingly, despite exhibiting a “coral-like” (Fig. S19) porous morphology there is substantial preferred orientation of the crystallite grains within this structure, as evidenced by the “pseudo”-single crystalline SAED pattern and the individual SEND patterns.

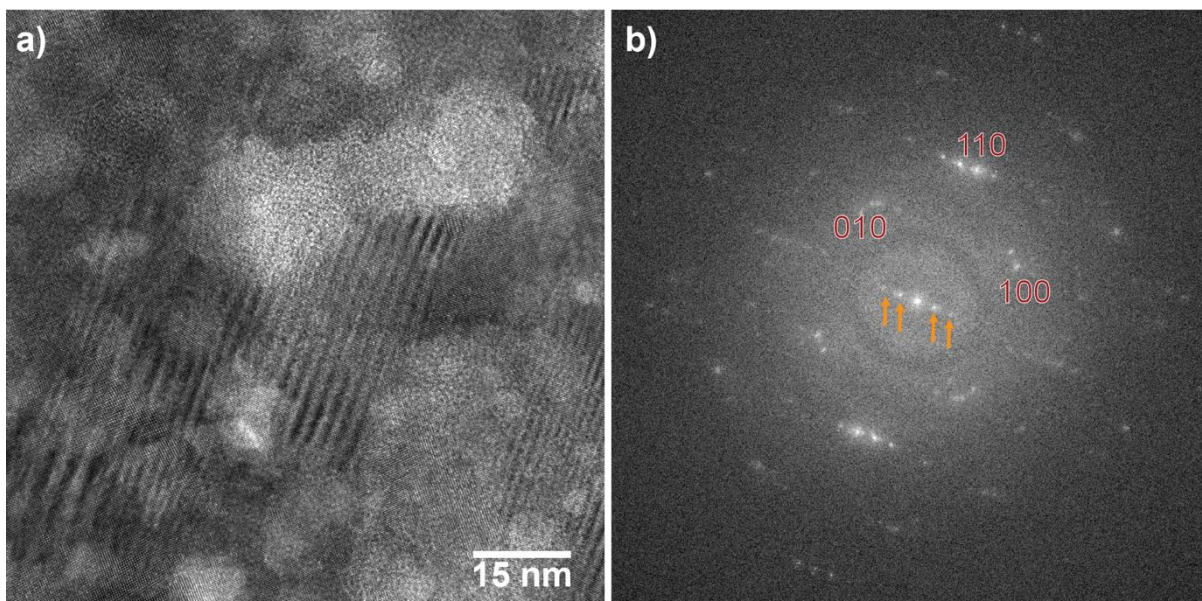


Fig. S23. TEM investigations of SU-100 powder soaked in KHCO_3 (aq) electrolyte. The “coral-like” structure was investigated further by means of HR-TEM. In a) a HR-TEM image is shown. The 100 and 110 spacings can clearly be identified. Moreover, there seems to be an approx. 2-2.2 nm periodic contrast variation occurring in some of the grains. The power-spectrum of the FFT shown in b) corroborates the SEND and SAED findings, and the major intensities can be indexed according to a [001] zone-axis pattern of $\text{Bi}_2\text{O}_2\text{CO}_3$. Furthermore, the FFT also reveals the aforementioned periodic contrast variations. These observations thus may be used to understand the origin of the satellite peaks observed in many SEND patterns (Fig. S21). The SEND study as well as the HR-TEM imaging indicate that the modulation only manifests itself in certain grains. Interestingly, there seems to be some coherence between the modulation in different grains across boundaries. However, it goes beyond the scope of this study to investigate the nature of these modulations further, e.g., determine if they are displacive or compositional in nature and if they are fully commensurate, incommensurate or if a continuum of different causes for this modulated intensity exists. Nonetheless, there may be some interesting relation to the parent SU-100 structure that may be unearthed in future studies.

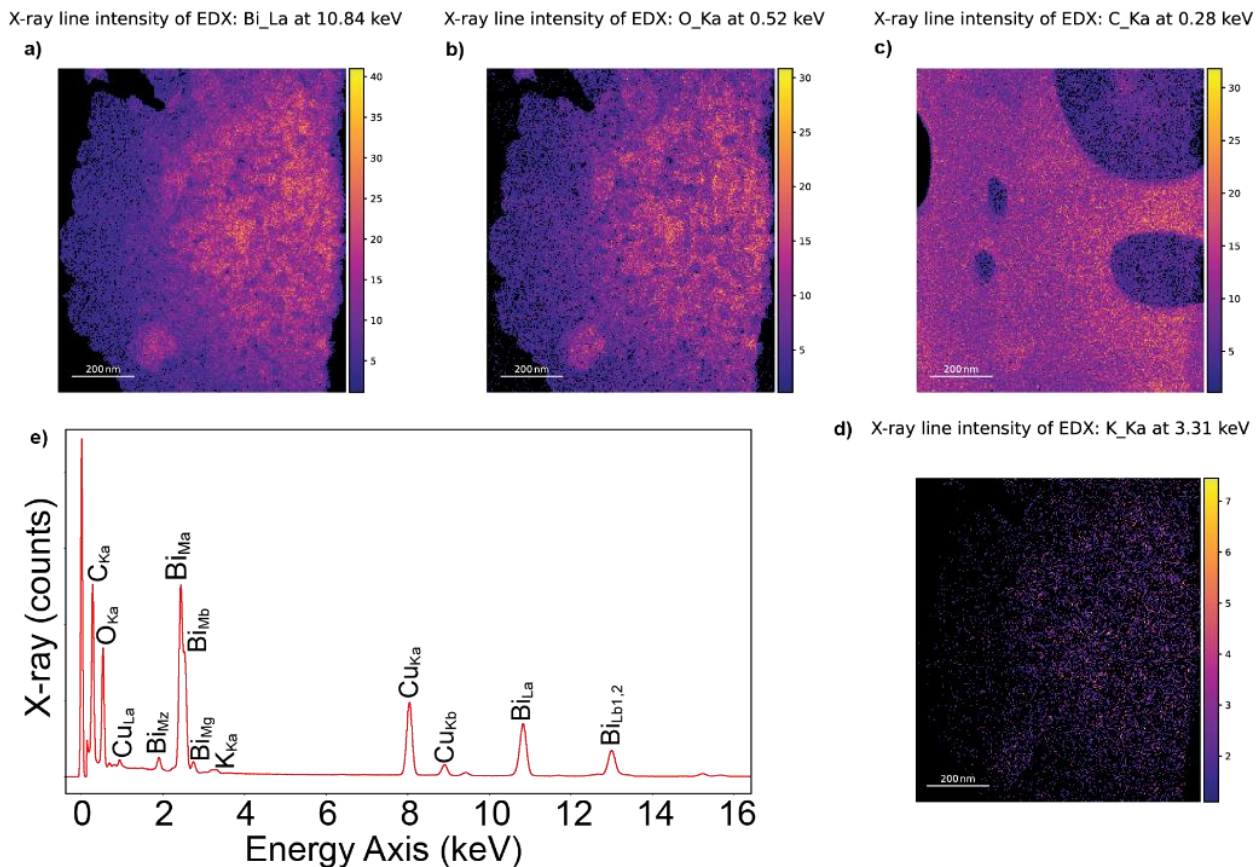


Fig. S24. EDX mapping of SU-100 powder soaked in KHCO_3 (aq) electrolyte. a-d) Maps of the X-ray counts (background corrected) for a) Bi-L α , b) O-K α , c) C-K α , d) K-K α . e) The summed spectrum of the entire sample with the major peaks indexed. Cu is due to the Cu grids used. A few unindexed peaks originate from the system, i.e. background peaks from Fe and Zr, others are minor peaks belonging to Bi. Based on fitting of the entire EDX spectrum a Bi/O ratio of approx. 0.37 was obtained. This ratio is relatively close to the 0.4 ratio expected for the $\text{Bi}_2\text{O}_2\text{CO}_3$, i.e., it falls within the expected uncertainty for these measurements, but is significantly lower than the ratio of 0.66 expected for Bi_2O_3 .

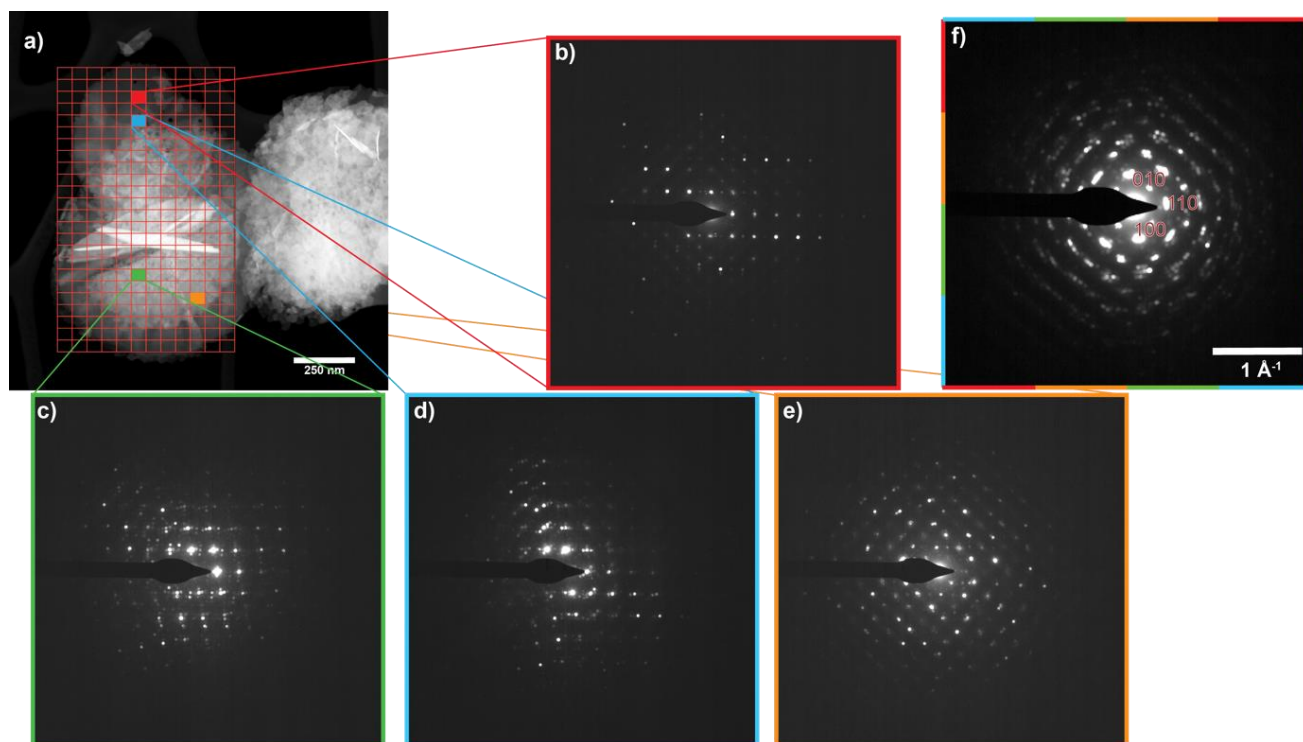


Fig. S25: TEM investigations of SU-100 powder soaked in KHCO_3 (aq) electrolyte. a) HAADF-STEM image with a grid overlaid to illustrate the scanning pattern employed for scanning electron nanobeam diffraction (SEND). The filled squares refer to selected probe positions from which the respective SEND patterns are shown in b)-e). The different area of the flower exhibit different orientations to a much larger degree than what was observed for the “coral / sponge” structure shown in Fig. S21. However, each individual “petal” seems to be pseudo-single crystalline in nature, i.e. different regions within the same petal show similar patterns except for what would be expected due to bending of the thin structures. Similar to what was observed in the sponge-like structure (Fig. S21 and S23), some areas exhibit satellite reflections indicative of complex structural features beyond the scope of this paper. The summed pattern shown in f) also has some similarities to the summed pattern shown in Fig. S21. Yet, it reflects the larger variation in orientations present in the scanned area by being closer to the ring pattern expected for completely randomly oriented crystallites.

X-ray line intensity of EDX: Bi_La at 10.84 keV X-ray line intensity of EDX: O_Ka at 0.52 keV X-ray line intensity of EDX: K_Ka at 3.31 keV

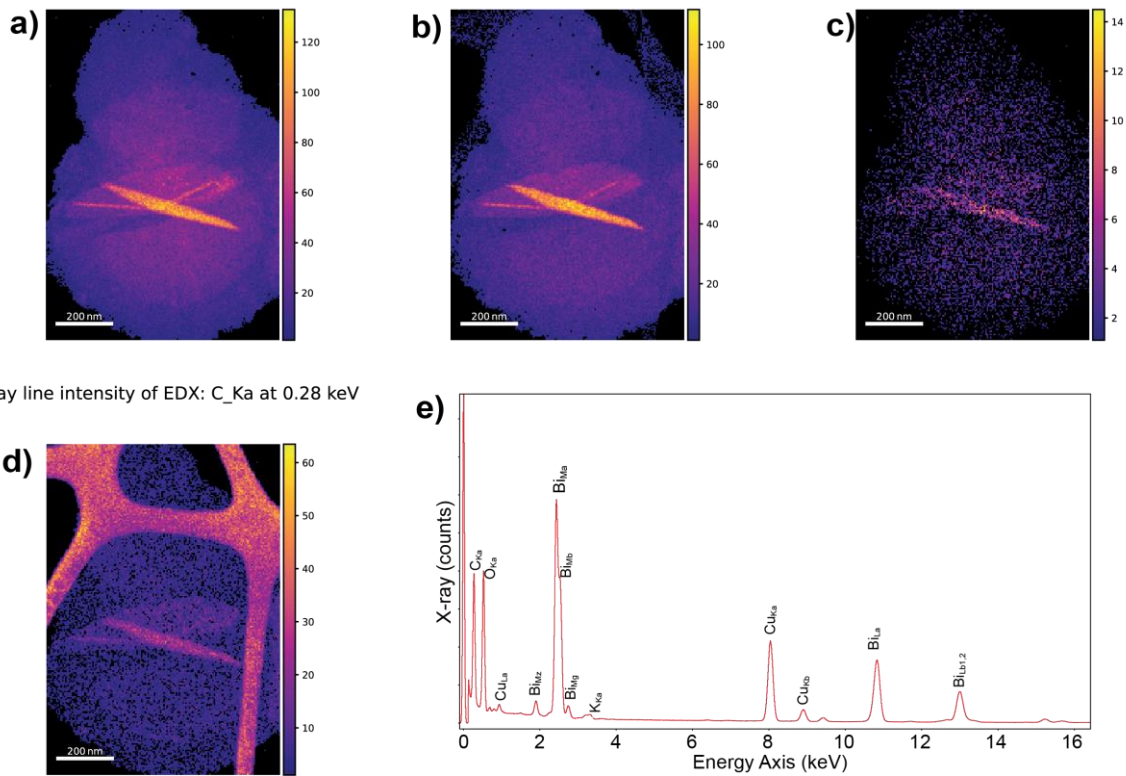


Fig. S26. EDX mapping of SU-100 powder soaked in KHCO_3 (aq) electrolyte. a-d) Maps of the X-ray counts (background corrected) for a) Bi-L α , b) O-K α , c) K-K α , d) C-K α . e) shows the summed spectrum of the entire sample with the major peaks indexed. Cu is due to the Cu grids used. A few unindexed peaks originate from the system, i.e. background peaks from Fe and Zr, others are minor peaks belonging to Bi.

3.3.4. Reduced SU-100 film

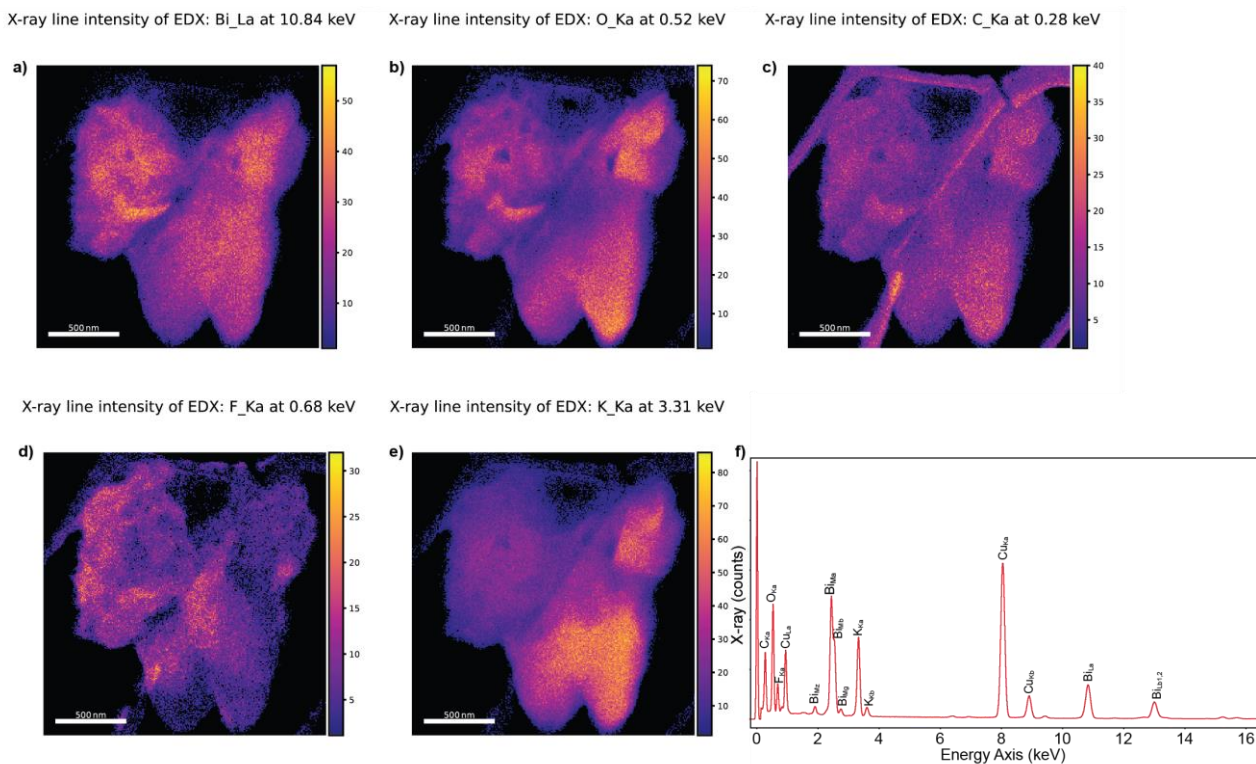


Fig. S27. EDX mapping of electroreduced SU-100: a-e) Maps of the X-ray counts (background corrected) for a) Bi-L α , b) O-K α , c) C-K α , d) F-K α , e) K-K α . f) shows the summed spectrum of the entire sample with the major peaks indexed. Cu is due to the Cu grids used. A few unindexed peaks originate from the system, i.e. background peaks from Fe and Zr, others are minor peaks belonging to Bi.

Non-negative matrix factorization (NMF):

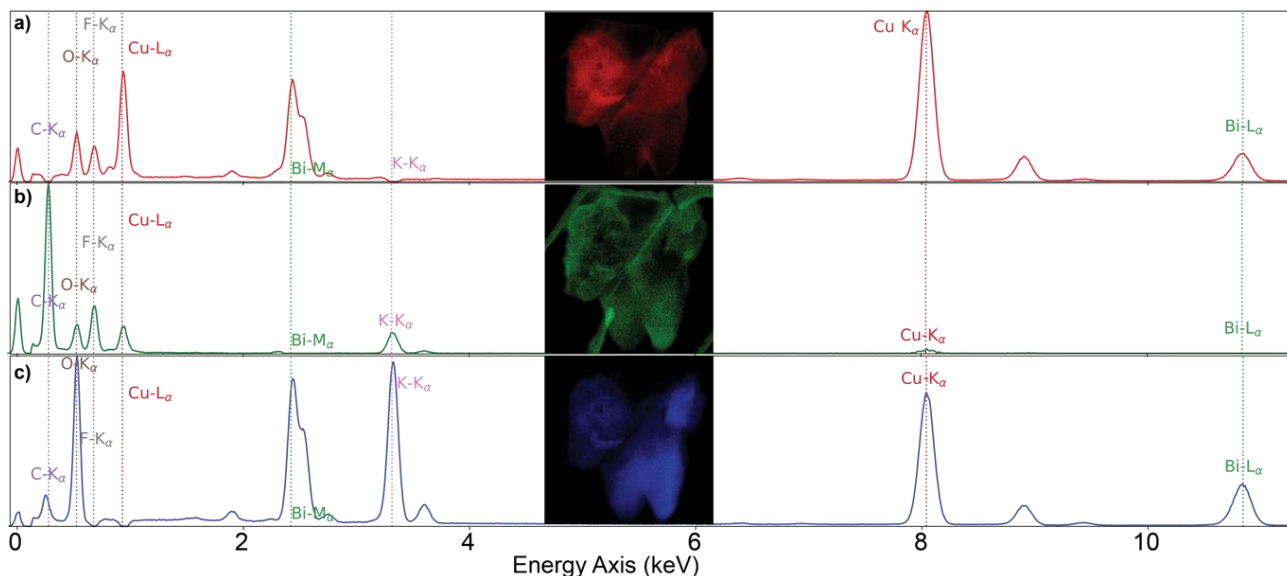


Fig. S28. NMF. The collected 3-dimensional (x and y probe position as well as an energy axis) STEM-EDX dataset was decomposed using the NMF decomposition algorithm implanted in Hyperspy. An output dimension of 4 was determined to be optimal. Three of the loadings, as well as factors, are shown here. The loading and factor not shown here was identified to describe the background and noise within the data.

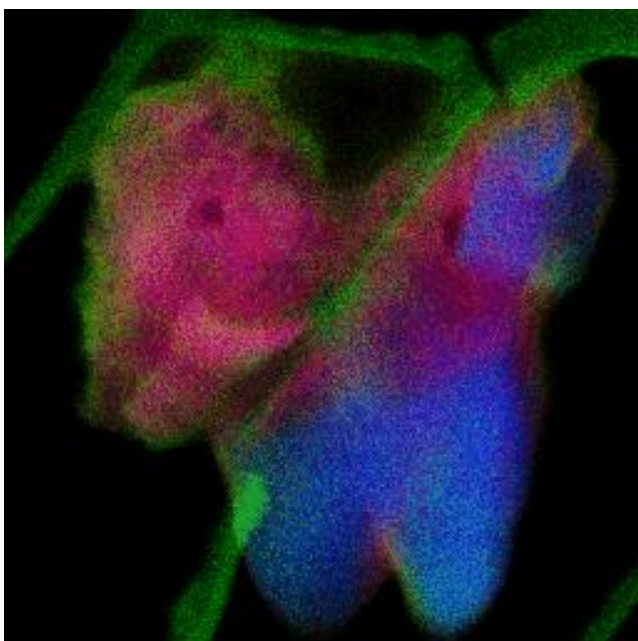


Fig. S29. RGB composite of the three NMF loadings. The green shell is high in F and low in Bi, and likely represents the Nafion coating the material. The majority of the K (expected to be present as residues from the electrolyte) is located at the lower right corner in the blue component, where the sample structure is more homogeneous. The red component is rich in Bi and resembles the flower like $\text{Bi}_2\text{O}_2\text{CO}_3$ structure morphologically.

3.4. X-ray absorption spectroscopy – linear combination analysis (LCA)

3.4.1. SU-100

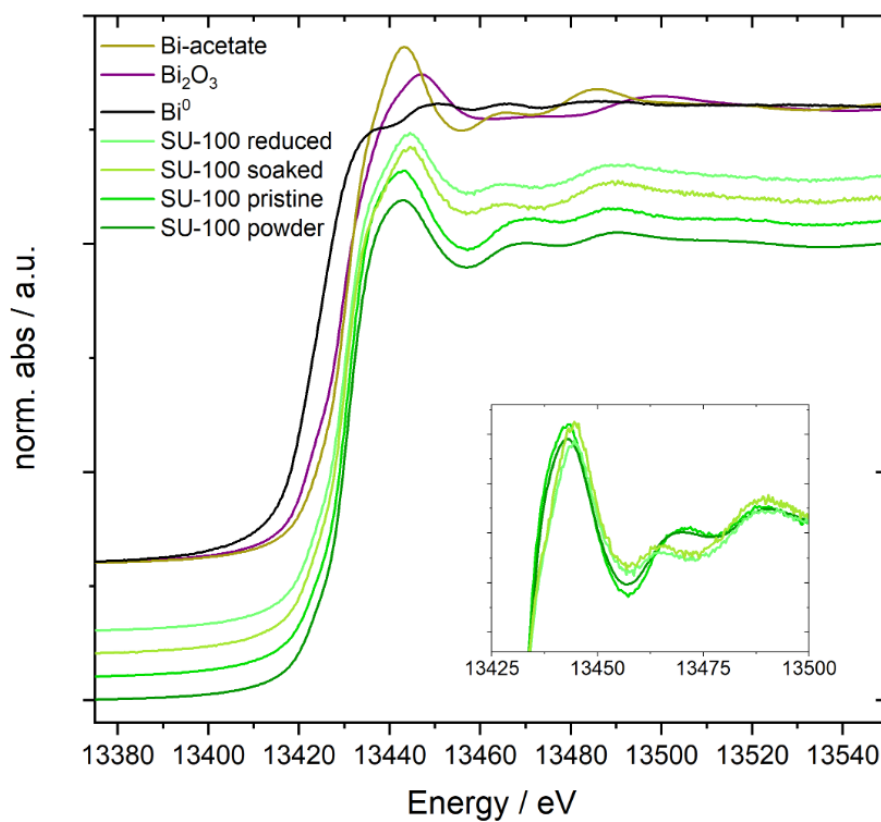


Fig. S30. XANES spectra of SU-100 powder and electrodes: pristine, soaked in KHCO_3 (aq) electrolyte for 15 min, and electroreduced at $-0.97 \text{ V}_{\text{RHE}}$ for 9 min. The spectra are compared with three standard samples: bismuth acetate, bismuth oxide, and metallic bismuth. The inset shows an overlay of the SU-100 data.

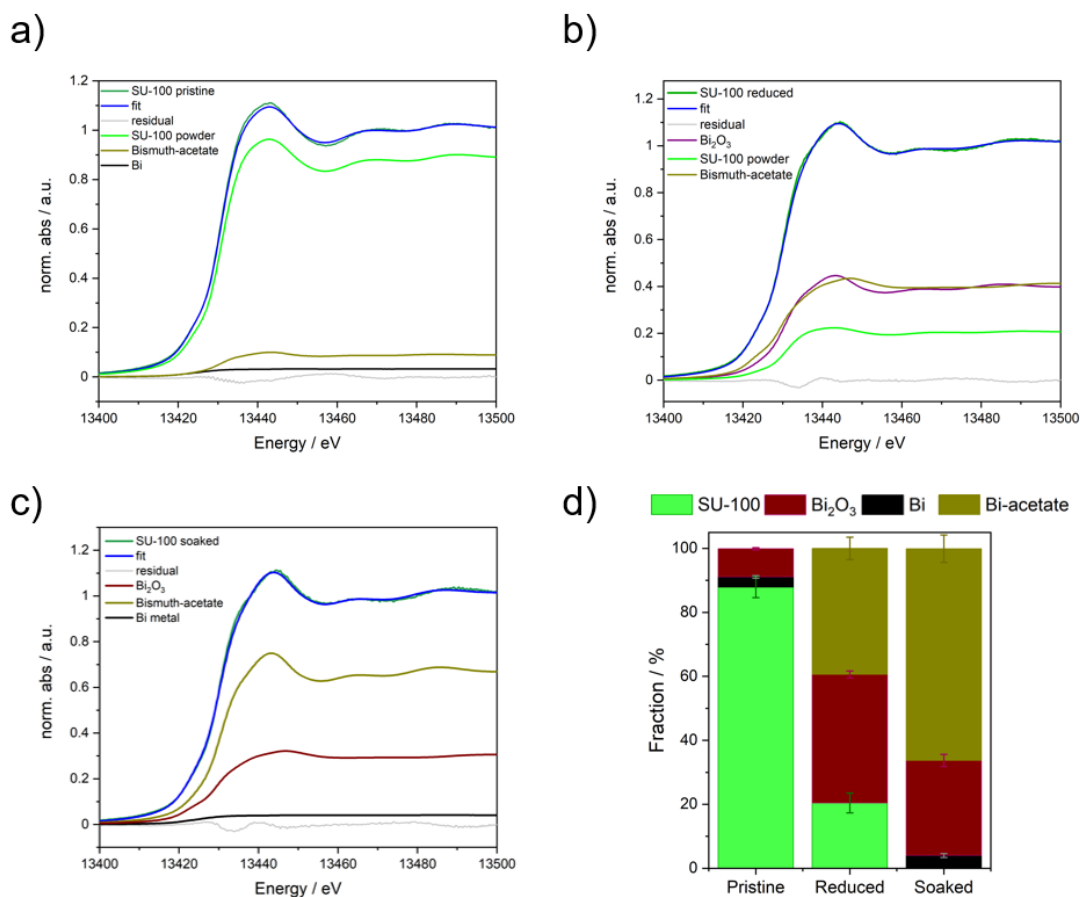


Fig. S31. LCA of SU-100 samples. a) Pristine electrode, b) an electroreduced electrode at $-0.97 V_{RHE}$ for 9 min, and c) a soaked electrode (15 min). A maximum of three standards were fitted to the spectra with constant E_0 . d) Results from the LCA. Fractions are given in atomic percentages of bismuth. Color code: SU-100: bright green, bismuth oxide: brown, bismuth acetate: olive, metallic bismuth: black.

The local structure of bismuth in the pristine SU-100 electrode can be described as a combination of 88(3) % (atomic percent) of the as-synthesized powder and some Bi₂O₃-like and Bi(0)-like coordination environment. Hence, the spectrum of the pristine electrode material (cast with Nafion solutions) is not perfectly described by the spectrum of the corresponding precursor powder (pressed as a pellet), corroborated by changes of SU-100 after film formation as observed by SEM (Fig. S16).

After reduction for 9 min at $-0.97 V_{RHE}$, only 20(3) % of the coordination environment around Bi can be described by the original SU-100 precursor structure. The rest can be described as approx. equal amounts of Bi₂O₃ and Bi(CH₃COO)₃. Soaking an electrode in 0.5 M KHCO₃ (aq) for 15 min without applying a potential completely destroys the SU-100 structure, and the coordination environment is best described as 66(4) % of bismuth acetate together with the oxide and a small amount of Bi(0). This supports the PXRD patterns after soaking (Fig. S20), where SU-100 is fully converted to crystalline Bi₂O₂CO₃ within 5 min. Unfortunately, we have no reference XANES spectrum of Bi₂O₂CO₃. However, in Bi₂O₂CO₃ there are two Bi(III) in the asymmetric unit, which each coordinate to seven oxygen atoms in Bi₂O₂CO₃.⁹ This is likely the reason that a mixture of Bi₂O₃¹¹ and Bi(CH₃COO)₃ reasonably fits data.

3.4.2. *Bi(btb)*

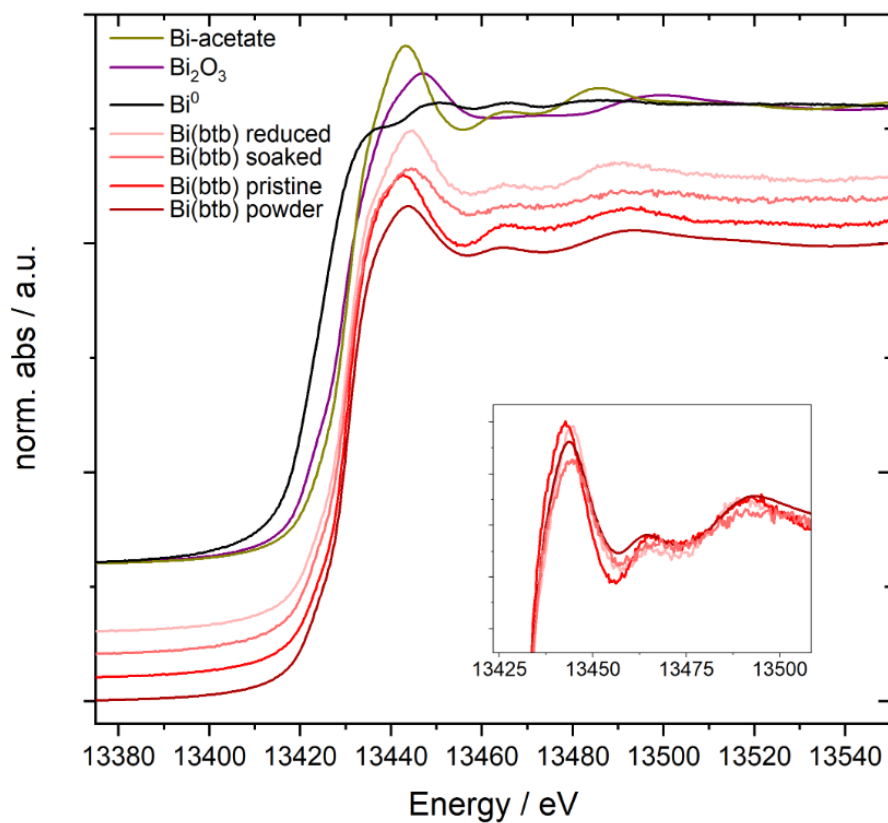


Fig. S32. XANES spectra of *Bi(btb)* powder and electrodes: pristine, soaked in KHCO_3 (aq) electrolyte for 15 min, and electroreduced at $-0.97 \text{ V}_{\text{RHE}}$ for 9 min. The spectra are compared with three standard samples: bismuth acetate, bismuth oxide, and metallic bismuth. The inset shows an overlay of the *Bi(btb)* data.

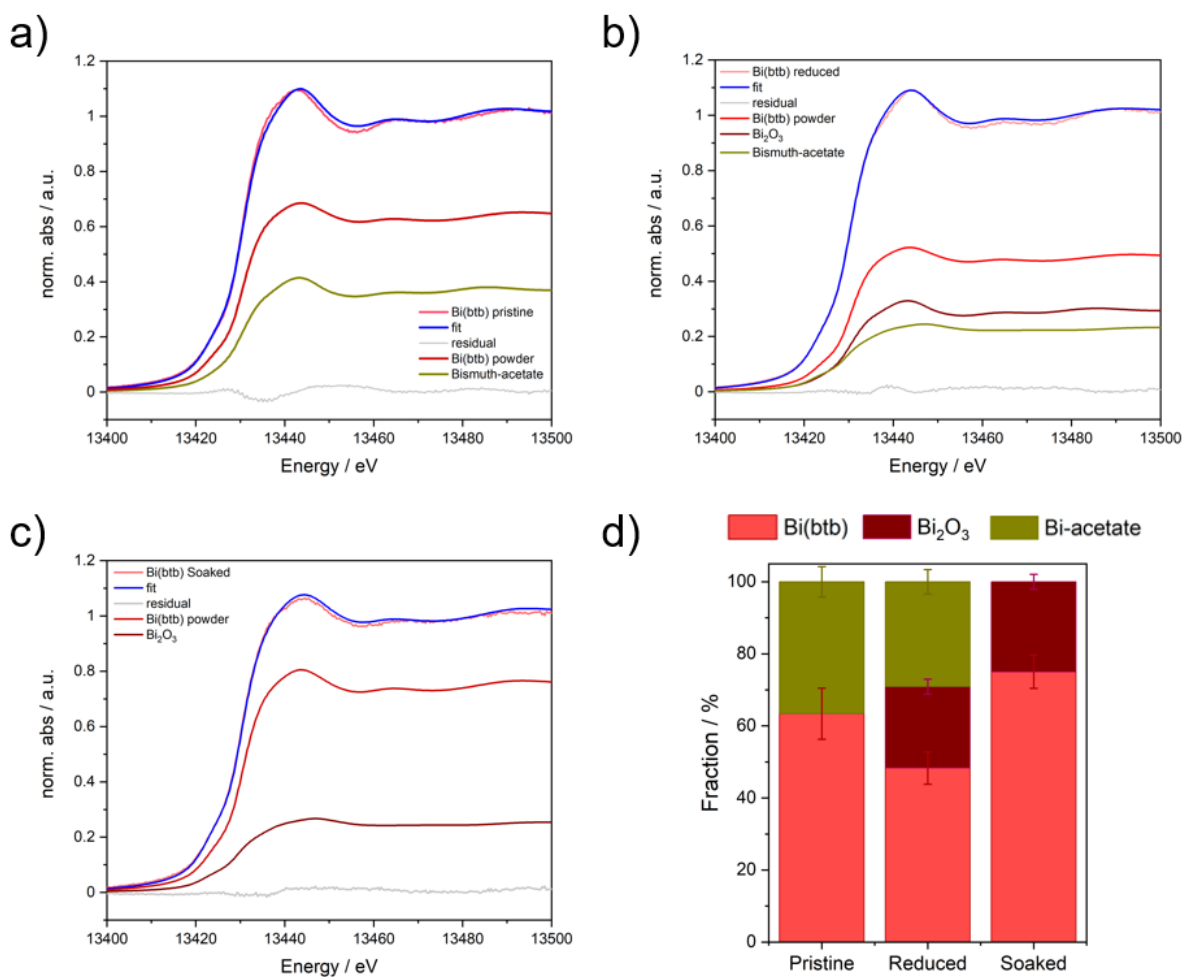


Fig. S33. Linear combination analysis (LCA) of Bi(btb) samples. a) Pristine electrode, b) an electroreduced electrode at $-0.97 V_{RHE}$ for 9 min, and c) a soaked electrode (15 min). A maximum of three standards are fitted to the spectra with constant E_0 . d) Results from LCA. Fractions are given in atomic percentages of bismuth. Color code: Bi(btb): red, bismuth oxide: brown, bismuth acetate: olive.

For Bi(btb), the structural transformation is also evident from the LCA results. As the coordination between Bi(III) and btb resembles the local structure of Bi(III) in bismuth acetate, the pristine electrode can be described as a combination of the two. A higher stability of Bi(btb) in the electrolyte in comparison with SU-100 in electrolyte is apparent with 75(5) % of the MOF being preserved after soaking for 15 min and 48(5) % after reduction. The larger relative chemical stability of Bi(btb) soaked in electrolyte is in agreement with PXRD data (Fig. S20).

3.5. Grazing incidence X-ray diffraction (GI-XRD)

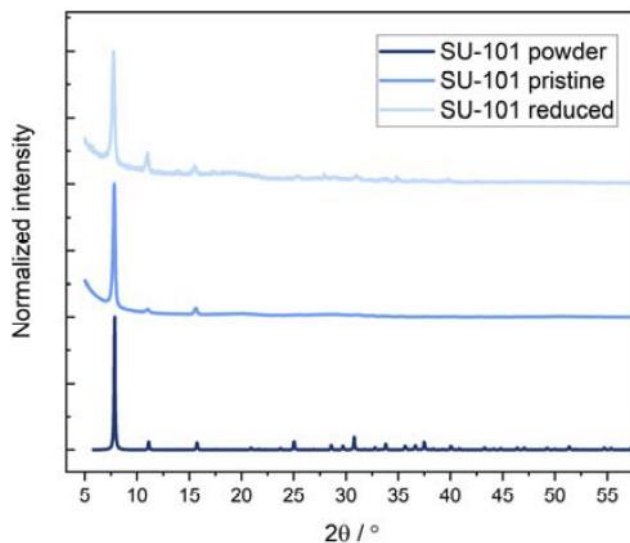


Fig. S34. GI-XRD data collected on SU-101 powder, a pristine electrode, and an electroreduced electrode at $-0.97 V_{RHE}$ for 30 min in CO_2 saturated $0.5 M KHCO_3$ (aq) electrolyte. The main peaks, hence the structure, are preserved at the operation conditions.

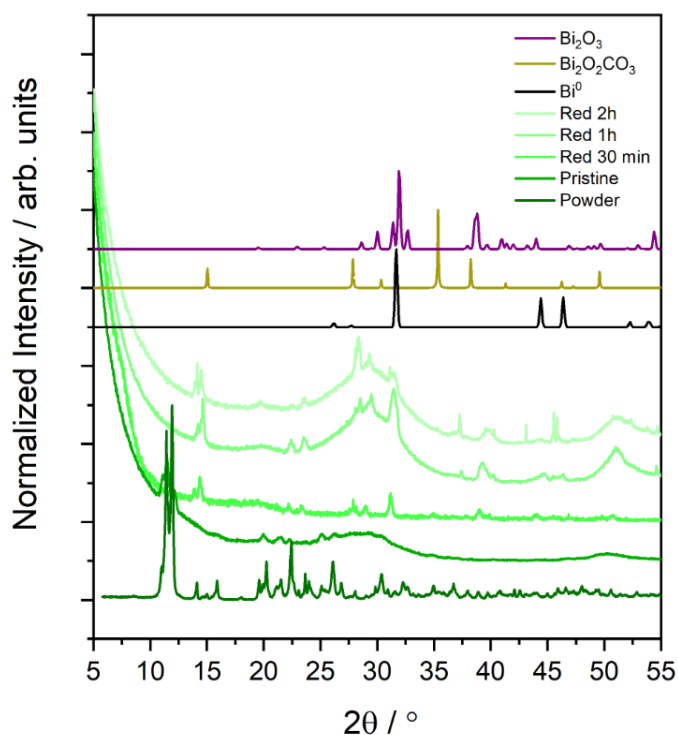


Fig. S35. GI-XRD patterns of SU-100 electrodes reduced at $-0.97 V_{RHE}$ for 30 min, 1 h, and 2 h respectively, and compared to the pattern of SU-100 and the calculated patterns of Bi_2O_3 ,¹¹ $Bi_2O_2CO_3$,⁹ and metallic Bi .¹² Only very small peaks are evident for the (013) reflection from the $Bi_2O_2CO_3$ phase at 35.5° . Additional unidentified Bragg peaks appear after 1 h and 2 h.

References

- 1 P. Lamagni, M. Miola, J. Catalano, M. S. Hvid, M. A. H. Mamakhel, M. Christensen, M. R. Madsen, H. S. Jeppesen, X. Hu, K. Daasbjerg, T. Skrydstrup, N. Lock, *Adv. Funct. Mater.*, 2020, **30**, 1910408.
- 2 M. Feyand, E. Mugnaioli, F. Vermoortele, B. Bueken, J. M. Dieterich, T. Reimer, U. Kolb, D. De Vos, N. Stock, *Angew. Chem., Int. Ed.*, 2012, **51**, 10373-10376.
- 3 E. S. Grape, H. Xu, O. Cheung, M. Calmels, J. Zhao, C. Dejoie, D. M. Proserpio, X. Zou, A. K. Inge, *Cryst. Growth Des.*, 2020, **20**, 320-329.
- 4 A. K. Inge, M. Ko, J. Su, M. Feyand, H. Xu, X. Zou, M. O'Keeffe, N. Stock, *J. Am. Chem. Soc.*, 2016, **138**, 1970-1976.
- 5 E. S. Grape, J. G. Flores, T. Hidalgo, E. Martínez-Ahumada, A. Gutiérrez-Alejandre, A. Hautier, D. R. Williams, M. O'Keeffe, L. Öhrström, T. Willhammar, P. Horcajada, I. A. Ibarra, A. K. Inge, *J. Am. Chem. Soc.*, 2020, **142**, 16795-16804.
- 6 Y. Wang, S. Takki, O. Cheung, H. Xu, W. Wan, L. Öhrström, A. K. Inge, *Chem. Commun.*, 2017, **53**, 7018-7021.
- 7 K. Momma, F. Izumi, *J. Appl. Crystallogr.*, 2011, **44**, 1272-1276.
- 8 M. J. Turner, J. J. McKinnon, D. Jayatilaka, M. A. Spackman, *CrystEngComm*, 2011, **13**, 1804-1813.
- 9 J. D. Grice, *Can. Mineral.*, 2002, **40**, 693-698.
- 10 hyperspy/hyperspy: Release v1.6.2, <https://zenodo.org/record/4683076#.YKY2j7UzZPY>, (accessed May 2021).
- 11 G. Malmros, L. Fernholt, C. J. Ballhausen, U. Ragnarsson, S. E. Rasmussen, E. Sunde, N. A. Sørensen, *Acta Chem. Scand.*, 1970, **24**, 384-396.
- 12 P. Cucka, C. S. Barrett, *Acta Crystallogr.*, 1962, **15**, 865-872.